3-1999

Characterization of the Double Scatter Spectrum in Multiplexed Compton Scatter Tomography

David W. Gerts

CHARACTERIZATION OF THE DOUBLE SCATTER SPECTRUM IN MULTIPLEXED COMPTON SCATTER TOMOGRAPHY

THESIS

David W. Gerts, Captain, USAF
AFIT/GAP/ENP/99M-03

DEPARTMENT OF THE AIR FORCE
AIR UNIVERSITY
AIR FORCE INSTITUTE OF TECHNOLOGY

Wright-Patterson Air Force Base, Ohio

Approved for Public release; distribution unlimited

AFIT/GAP/ENP/99M-03

CHARACTERIZATION OF THE DOUBLE SCATTER SPECTRUM IN MULTIPLEXED COMPTON SCATTER TOMOGRAPHY

THESIS

Presented to the Faculty of the Graduate School of Management

And Engineering of the Air Force Institute of Technology

Air University

Air Education and Training Command

In Partial Fulfillment of the Requirements for the

Degree of Master of Science

David W. Gerts, B.S., B.S.

Captain, USAF

March 1999

AFIT/MS/ENG/99M-03

DOUBLE SCATTER SPECTRUM FOR THE MULTIPLEXED COMPTON SCATTER TOMOGRAPH

David W. Gerts, B.S., B.S
Captain, USAF

Approved: Date:

Jeffrey B. Martin — 8 Mar 99
Major Jeffrey B. Martin, Ph.D., USAF
Chairman, Advisory Committee

Kirk A. Mathews — 5 Mar 1999
Kirk A. Mathews, Ph.D.
Member, Advisory Committee

Larry W. Burggraf — 8 Mar 1999
Larry W. Burggraf, Ph.D.
Member, Advisory Committee

Acknowledgements

I would like to acknowledge my advisor, Major J. Martin, for his support and encouragement. Additionally, I gratefully acknowledge the aid and patience of Dr. K. Mathews as well as the continued discussions with Dr. L. Burggraf. Finally, I would like to thank Captain B. Evans and Captain M. Sands for their help throughout the project.

Most importantly, I would like to thank my wife, Amy, and my son, Dax, for their unrelenting support during this thesis. The long hours and diligent studies would not have been possible without the support of my wife. My accomplishments are only so much greater due to her love and continued devotion.

David W. Gerts

Table of Contents

List of Figures

List of Tables

Abstract

The Multiplexed Compton Scatter Tomograph (MCST) uses single back-scattered photons to image electron density in aluminum. A source of error in this imaging technique is the presence of multiple scatters. This thesis studies the double scatter spectrum as an approximation of the multiple scatter spectrum. A deterministic code called Monte Carlo Double Scatter (MOCADS) was developed to investigate the double scatter spectrum.

The code includes calculations of the Rayleigh scatter, Compton scatter, Doppler broadening effects of the spectrum, and polarization effects following the Compton scatter. The Doppler broadening portion of the code was validated by a deterministic code called Scatgram. The mechanics of double scatter were validated by a Monte Carlo transport code. And all included features in the code were validated by a laboratory experiment.

The MOCADS code was used to simulate an experiment where a void was present in the sample and compared to a solid sample. The simulation showed that the shape of the double scatter spectrum did not depend on the presence of the void. Another simulation examined the effects of polarization and Doppler broadening. These two effects were shown to significantly influence the shape of the spectrum. Finally, a laboratory experiment was examined where the single scatter estimate was improved by the removal of the double scatter spectrum from the total spectrum.

CHARACTERIZATION OF THE DOUBLE SCATTER SPECTRUM IN MULTIPLEXED COMPTON SCATTER TOMOGRAPHY

Chapter 1: Background

Regularly, the Air Force must examine its aircraft for defects, faults, and corrosion. All aircraft must be regularly inspected as being capable of withstanding the strains of flying. However, it can be very difficult to locate hidden corrosion. The standard method of locating hidden corrosion has been to directly inspect the aircraft by disassembling its component parts that can be quite destructive to the aircraft. It may be possible to locate corrosion regions in a non-invasive, non-destructive manner using back-scattered gamma rays.

In order to examine the use of back-scattered gamma rays to find corrosion, the Air Force Research Laboratory commissioned AFIT/ENP to build a first generation Multiplexed Compton Scatter Tomograph (MCST). The object of this MCST device is to show that the concept of backscatter imaging with gamma rays can be accomplished.

The MCST is presently being tested to show its capability to accurately image a given object. The initial investigation indicates that the MCST

concept works using a single detector array. Yet, the desired final result of this research would be a device that could detect corrosion on an airplane. A new MCST would have to be built because the present system only images a small region. As a consequence, several complications would arise. One such complication may be the increased abundance of multiple scatters in the imaging signal. Thus, investigating the effects of multiple scatters is a step toward constructing a better device.

This research characterized the double scatter spectrum. The goal was to understand the shape of the double scatter spectrum. With the shape of the double scatter spectrum characterized, it can be removed from the total spectrum. And, removing the double scatter spectrum from the total spectrum creates a better estimate of the single scatter spectrum.

To better understand the purpose of examining the double spectrum, it is important to study the basic setup of the MCST. A very brief description of the MCST follows in Section 1.1. The scope of the research follows the brief description of the MCST. Finally, the further development of the remainder of the thesis is covered.

Section 1.1: MCST Project Description

The MCST device is based on a correspondence between the detected gamma energy and the angle through which that gamma ray scattered. Energy measurements localize the scattering position and the incoherent

scattering interaction coefficient is proportional to the electron density. An algorithm has been developed by Captain B. Evans that can use this correspondence in conjunction with a known experimental geometry in order to image a given object's electron density. This electron density is proportional to the actual material density. Based on the material density, then, the MCST indicates where a void or some corrosion in the aluminum is located.

The current MCST system is composed of a source, source collimator, sample, detector collimator, and detectors. A typical arrangement is shown in Figure 1. The remainder of the MCST system acquires the data collected by the detectors and recreates the image of the sample based on the electron density.

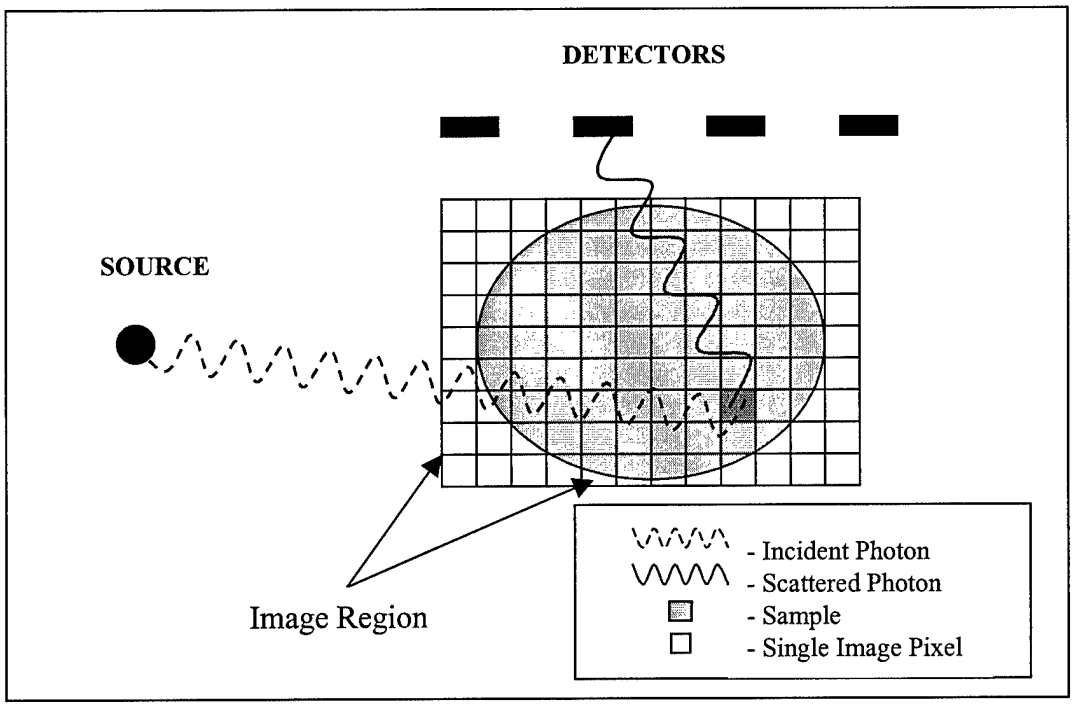

Figure 1: Sample geometry for MCST system [Figure provided courtesy of Captain M. Sands]

The major geometrical consideration of the MCST for this research is the fan-beam collimation of both the source and the detector. If either of the collimators were widened in the system, the ratio of the number of multiple scatters to the number of single scatter would increase in the signal. The main advantage of MCST over conventional X-ray backscatter imaging is efficiency. Yet, if the collimators cannot be removed, then the technique has achieved little progress towards improving the efficiency of imaging objects. And, if either of these collimators is removed, the MCST will need to correct for the presence of multiple scatters.

Section 1.2: Scope of Research

This research is intended to characterize the double scatter spectrum. It is assumed that the double scatter spectrum is the next most important sub-spectrum after the single scatter sub-spectrum in the total spectrum. A computer modeled was created to characterize the double scatter spectrum. This model was based on a deterministic formulation that utilized a Monte Carlo integration over the six or eight dimensional integral. The code was called Monte Carlo Double Scatter (MOCADS).

Since double scatter has not been directly solved for any similar situation, many various sources were needed to create the MOCADS code. Although many authors have examined multiple scatters, few have tried to

characterize the spectrum. Instead, most authors examine multiple scatters with the goal of simply minimizing the total number of multiple scatters. To accomplish this minimization, it is sufficient to only count the total number of multiple scatter events. For this research, however, the actual double scatter spectrum is needed. Thus, this research required a wholly new approach.

MOCADS needed to be validated to confidently predict the double scatter spectrum. Since no known code existed that modeled all the features in MOCADS, its validation required several separate steps. MOCADS was compared to two other computer models in order to validate portions of the code. These two codes are considered to be valid for the calculations of interest for comparing to MOCADS. A laboratory experiment was also designed and performed to examine the multiple scatter spectrum. A MOCADS simulation was validated against this experiment.

Having validated the MOCADS code, double scatter spectra were examined to determine the impact of a void on the spectra. Two possibilities could occur. One, the shape of the double scatter spectra could be influenced by the presence of the void—and thus contain information. Or, the shape could be essentially independent of the presence of a void. If the shape of the double scatter spectrum does not change if the sample has a void, then it should be possible to remove the double scatter spectrum *blindly* from a laboratory measurement and improve the single scatter spectrum. *Blind* removal means that the presence of the void was not known a priori. Thus, if

the double scatter spectrum can be simulated regardless of the void, then the single scatter spectrum can be improved in all cases.

The complicating factors of Doppler broadening and polarization were also examined to determine whether or not they had major effects on the final double scatter spectrum. In addition, another laboratory experiment was undertaken to determine whether the simulated double scatter spectrum could be used to better estimate the single scatter spectrum.

Section 1.3: Document Layout

In chapter two, the theory of scattering is developed. Initially, the basis for single scatter is developed including Doppler broadening. Starting from single scatter, the physics behind double scatter is examined. Double scatter has the additional complication of polarization following the first Compton scatter. Additionally, the polarization formulation and its impact on the double scatter spectrum are discussed.

In chapter three, the implementation of the computer code is discussed. A deterministic code called Monte Carlo Double Scatter integration (MOCADS) is developed. This code is based on the principle of Monte Carlo integration of a deterministic integral. The various assumptions concerning the implementation are discussed.

Chapter four details the tools used to validate the MOCADS code. The experiment and experimental apparatus used to validate MOCADS is

described. Also, the implementation of a Monte Carlo transport code called Monte Carlo Neutron-Photon Transport (MCNP) is presented. MCNP is a well-documented transport code that was used to validate portions of the deterministic code. In addition, an experimentally validated code called Scatgram, developed by Captain B. Evans, is presented. Scatgram is a deterministic code that uses a discretized mesh to calculate the single scatter spectrum.

The MOCADS code is validated in chapter five. The validation uses the codes and experiment described in chapter four. The MOCADS code is validated with respect to the overall shape of the single and double scatter predictions, albeit with some reservations. The inconsistencies between the validation codes and MOCADS are presented.

MOCADS simulations follow in chapter six. These simulations characterize the double scatter spectrum and the important physic's theory necessary to include in the model. Additionally, a comparison is made between a laboratory experiment with a known geometry and a MOCADS simulation of the geometry.

The conclusions and further recommendations follow in chapter seven. Although the MOCADS code contained a few discrepancies between the validation codes, the simulation accurately characterized the double scatter spectrum. The double scatter spectrum does not contain any significant dependence on the presence of a void.

Chapter 2: Theory

In order to model multiple scatters within the sample, a first order approximation is made. The twice-scattered photons are considered as the dominant factor in the multiple scatter spectrum. This approximation is justified because the ratio of the single scattered photons to the twice scattered photons is roughly the same as the ratio of the twice to the three times scattered photons [Felsteiner, 1974]. As well, the percentage of the single scattered photons to the double scattered photons is approximately 3~10%, depending upon the specific geometry chosen [Felsteiner, 1974]. Thus, to first order, it suffices to examine the double scatter contribution to the overall spectra.

As a basis for studying the double scatter spectra, the physics of single scatter must be understood since double scatter consists of a series of two single scatters. This series of single scatters, however, is not truly independent. Yet, it is important to examine the simpler case of single scatter before adding the complication of the correlation between the first and the second scattering events. Additional complications arise due to two different forms of scattering possible at the energy range of interest—Rayleigh scattering and Compton scattering.

Both Rayleigh and Compton scattering involve the scatter of a photon from an electron. Rayleigh scattering is coherent scatter, by which we mean that the photon does not lose any energy to the electron. In contrast, Compton scattering is an incoherent scatter whereby the photon loses energy, and the electron is ejected from its bound atomic orbital.

Section 2.1: Single Scatter Physics

In 1929 Klein and Nishina derived a formula from Quantum Electrodynamics (QED) to describe the differential cross section of Compton scatter. Latter, the theory of Rayleigh scattering was developed under the theory of QED. Unlike the Klein-Nishina formula, however, the Rayleigh scatter formula consists of an experimentally measured factor multiplied by a theoretically derived function. Thus, it is necessary to examine both types of scatter independently.

Compton Scatter

Compton's theory of incoherent scatter is based on the assumption that a photon strikes an electron at rest. The case of a moving, non-accerating electron can be obtained from this special case by a Lorentz transformation [Evans, 1955]. This is typically called the relativistic form for the Compton equation. This correction is not necessary for electrons with a small amount

of kinetic energy (typical velocities less than 0.1 times the speed of light). For the Klein-Nishina formulation, the struck electron is considered to be unbound as well. These approximations hold for many cases of Compton scatter since the photon energy is usually much larger than the binding energy of the electron. Yet, the approximation of the bound electron is not entirely valid at the energy range of interest. The relativistic correction, however, is not used since the electrons have little kinetic energy prior to the interaction in relation to the photons of interest; typically electrons have less than 1 to 2 keV of kinetic energy. This is non-relativistic as the electron rest mass is 511 keV/c^2.

In the approximation of an unbound electron, the Compton scattered photon has a uniquely defined energy [Evans, 1955]. The energy of the photon following a scatter is related to the initial energy by

$$\omega' = \frac{\omega}{1 + \frac{\omega}{m_e c^2}(1 - \cos\theta)} \qquad (1)$$

where

ω : intial energy,

ω' : final energy,

m_e : rest mass of the electron,

c : speed of light

θ : Compton scatter angle.

The geometry for the Compton scattering is given below. The angle for the scatter is measured relative to the direction of the incident photon and the energy of the scatter photon is determined from the equation above. The

Compton equation is an approximation that works very well if the photon energy is above a few hundred keV.

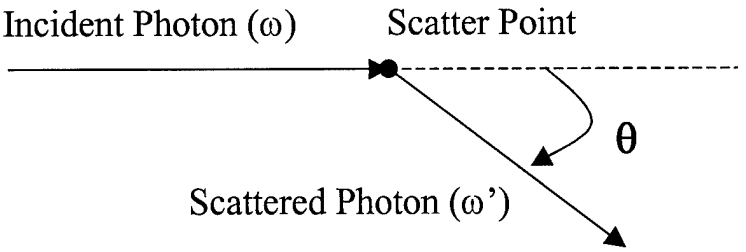

Figure 2: Compton Scatter Geometry

The Compton scatter has a cross section which is angularly dependent. The Klein-Nishina cross section for polarized and non-polarized radiation are given in equations (2) and (3). The Klein-Nishina relation predicts a more forward biased cross section as the energy of the incident photon increases [Evans, 1955]. This differential cross section per differential solid angle for polarized photons is

$$\frac{d\sigma_{CS}}{d\Omega} = \frac{r_0^2}{2}\left(\frac{\omega'}{\omega}\right)^2\left(\frac{\omega'}{\omega}+\frac{\omega}{\omega'}-2\cos^2\xi\right) \qquad (2)$$

where

r_0^2 : classic electron radius,

ξ : angle between ε and direction of scatter,

ε : electric vector of incident photon.

The non-polarized Klein-Nishina formula is a very similar equation except that the angular dependence of the cross section is no longer dependent on the incident photon polarization. Instead the polarization of the incident photon has been averaged over all possible polarization orientations to give a non-polarized Klein-Nishina relation.

When a collection of photons have no known polarization dependence, then the collection is known as non-polarized photons. A photon that is a member of this collection of non-polarized photons is itself said to be non-polarized. A mathematical representation of this collection of non-polarized photons is averaging over all possible polarization orientations. Mathematically describing polarization is similar to describing a point in space—it requires only two coordinates. To describing a photon's polarization, it requires only a linear combination of two unit, perpendicular vectors representing the polarization. The average is taken over two perpendicularly polarized photons [Evans, 1955]. This average gives the non-polarized Klein-Nishina relation as

$$\frac{d\sigma_{CS}}{d\Omega} = \frac{r_0^2}{2}\left(\frac{\omega'}{\omega}\right)^2\left(\frac{\omega'}{\omega}+\frac{\omega}{\omega'}-\sin^2\theta\right) \qquad (3)$$

where

θ : angle between incident and scattered photon.

Figure 3 shows the non-polarized Klein-Nishina relation plotted for various photon energies versus the angle of scatter. The energy of the photon is represented as α, which is the photon energy in units of electron rest mass. In the case of the 88.03 keV photon of interest, α is equal to 0.17 $m_e c^2$.

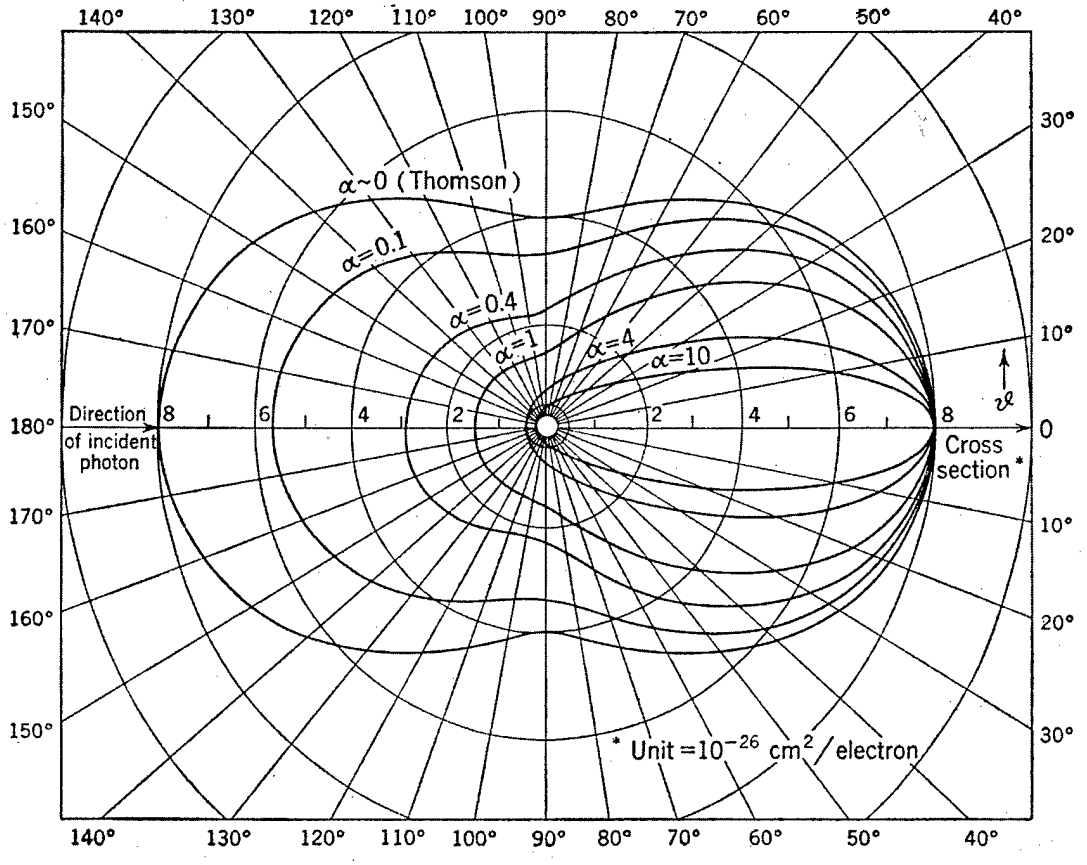

Figure 3: Klein-Nishina Relation for the Number of Photons Scatter into Unit Solid Angle at a Mean Scattering Angle ϑ [Figure from Evans, 1955]

The one-to-one correspondence between the energy and the angle in the Compton equation is important to the development of the MCST. If a mono-energetic source were used to illuminate a sample, the Compton relation would allow the researcher to determine the angle through which the gamma ray scattered by measuring the final energy. Thus, the Compton equation is very useful to determine the electron density by examining the relative intensity of the different angular contributions. Unfortunately, the Compton equation is only an approximation and the Doppler broadening formulas developed later will be needed to correct for the movement of the

bound electron. This correction will remove the one-to-one exact correspondence, but the correspondence is still nearly one-to-one.

To describe the angular dependence, the polarized Klein-Nishina formula describes the interaction if the incoming photon is polarized. If the incident photons are polarized, the scattered photon has only a certain probability of having the same polarization—it thus become non-polarized. The probability of the outcoming photon becoming non-polarized is [Namito, 1993]

$$\left(\frac{\omega'}{\omega}+\frac{\omega}{\omega'}-2\right)\Big/\left(\frac{\omega'}{\omega}+\frac{\omega}{\omega'}-2\sin^2\theta\cos\Phi\right) \qquad (4)$$

where

Φ : azimuthal scattering angle,

θ : scattering angle.

Since photons emitted from a radioactive decay do not have any known polarization, however, the case when the incident photons are not polarized is considered. The non-polarized photons become partially polarized. The amount of partial polarization is determined by the azimuthal angle of the Compton scatter. Thus, when the second scatter occurs, the new partial polarization of the photons and their azimuthal dependence need to be accounted for in the equations calculating the probability of a double scatter.

Impulse Approximation to Compton Scatter

The Klein-Nishina formula is only an approximation based on a free, or unbound, electron scattering incoherently with a photon. Yet, the electron is bound in the atom. The impulse approximation was developed to handle the assumption of a bound electron with non-zero momentum in the Klein-Nishina formulation for Compton scatters. The impulse approximation approximates the effect of the bound electron as though the electron either imparts or removes a small amount of energy from the photon from what the Compton relation predicts. By including the momentum of the electron in the electron-photon interaction, the final result is a broadening of the expected energy of the photon. This broadening of the photon due to the momentum of the bound electron is often referred to as the Doppler broadening.

Starting in 1975, Ribberfors developed several formulations for treating the bound electron—photon interaction. The first development was the relativistic impulse approximation, in which Ribberfors assumed that the motion of the electron needed to be completely accounted for in the approximation. This formulation assumed that the incoming photons were not polarized. The relativistic formulation is shown simply for the complete progression of the impulse approximation. In the following equation for the impulse approximation, the units of the equations have been scaled such that $c = 1$ and $h/2\pi = 1$. The relativistic equation is

$$\frac{d^2\sigma}{d\omega'\,d\Omega} = \frac{r_0^2 m_e^2 \omega'}{2\omega\left|\vec{k}-\vec{k}'\right|\left(m_e^2+p_z^2\right)^{1/2}}\,\overline{X}(R,R')J(p_z) \qquad (5)$$

where

$$\overline{X}(R,R') = \frac{R}{R'}+\frac{R'}{R}+2m_e^2\left[\frac{1}{R}-\frac{1}{R'}\right]+m_e^4\left[\frac{1}{R}-\frac{1}{R'}\right]^2,$$

$$R = \omega\left[\left(m_e^2+p_z^2\right)^{1/2}+\frac{(\omega-\omega'\cos\theta)p_z}{\left|\vec{k}-\vec{k}'\right|}\right],$$

$$R' = R-\omega\omega'(1-\cos\theta),$$

$$\left|\vec{k}-\vec{k}'\right| = \left[\omega^2+(\omega')^2-2\omega\omega'\cos\theta\right]^{1/2},$$

$$p_z = \frac{[\omega\omega'(1-\cos\theta)-m(\omega-\omega')]}{\left|\vec{k}-\vec{k}'\right|},$$

$J(p_z)$: experimentally determined Compton profile,

θ : scattering angle.

The Compton profile is sharply peaked at the energy predicted by the Compton equation. Figure 4 shows the profile versus the p_z value as defined in the equation above. The p_z value is related to the electron momentum with reference to the direction of the incident photon. The p_z is averaged over all of the electron shells for the particular element of interest to give a table of values of p_z versus $J(p_z)$. Of practical interest is that the Doppler broadening removes the one-to-one correspondence of the energy to the angle of scatter. The impulse approximation is a potential solution to describe the Doppler broadening. The impulse approximation calculation show that the energy can vary ~2 keV with the same angle of scatter.

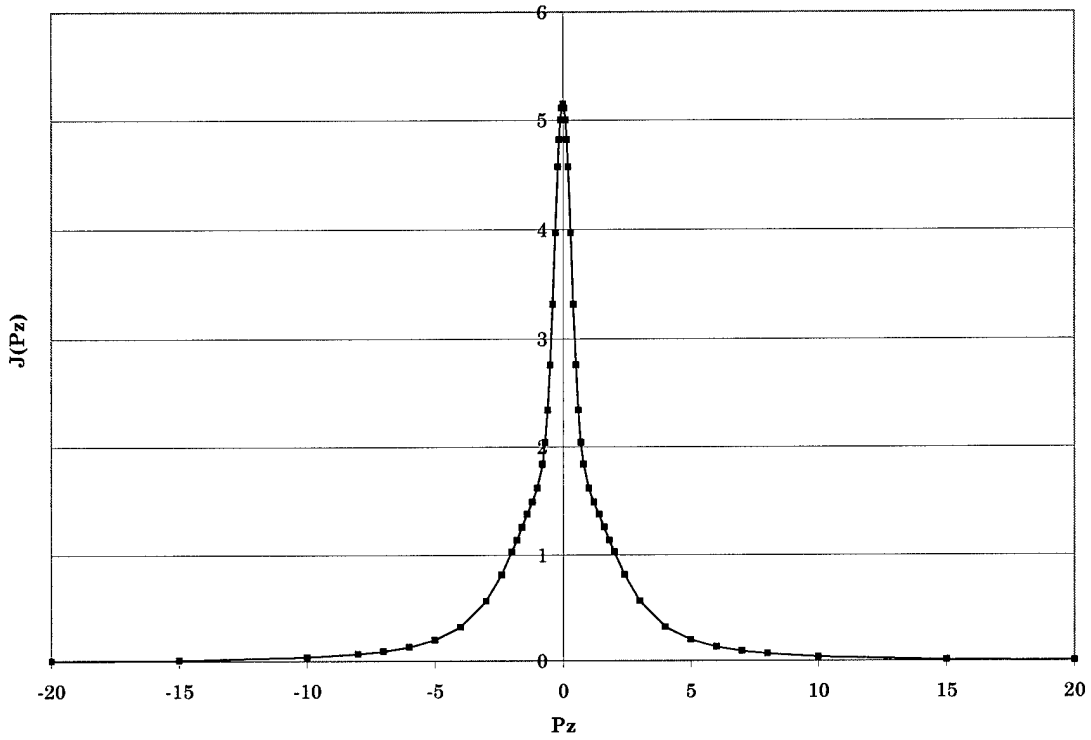

Figure 4: Compton Profile for Aluminum [Data from Biggs, 1975]

The relativistic form is useful for higher energy photons. This correction was not necessary to include since the relativistic theory is not needed for photons of energy less than 100 keV [Ribberfors, 1982]. The Compton profile will still be used, albeit not in the relativistic form.

Ribberfors developed the next formulation in 1975 for polarized photons. This approximation assumed again that the photon was bound with the inclusion of relativistic effects. In Ribberfors' development of the polarized impulse approximation, the equations are very similar to the Klein-Nishina formulation, except for the inclusion of the Compton profile term [Ribberfors, October 1975]. This similarity shall be used to good effect in the

development of the double scatter formulas. The polarized impulse approximation equation is

$$\frac{d^2\sigma}{d\omega' d\Omega} = \frac{r_0^2 m_e \omega'}{2\omega\left|\vec{k}-\vec{k}'\right|}\overline{X}(R,R',\xi)J(p_z) \qquad (6)$$

where

$$\overline{X}(R,R',\xi) = \left(\frac{R}{R'}+\frac{R'}{R}-1+2\cos^2\xi\right), \text{and}$$

$R, R', \left|\vec{k}-\vec{k}'\right|, J(p_z)$ are defined above with

ξ : angle between incident electric vector and the direction of scatter.

Finally, in 1982, Ribberfors developed the non-relativistic impluse approximation to the Klein-Nishina formula. This approximation to the relativistic equation is valid when there is low energy and momentum transfer to the electron [Ribberfors, 1982]. And, an 88.03 keV photon is considered to be a low-energy gamma because the ratio of the energy to the rest mass of an electron is 0.17. Since this ratio is less than 1, the total energy and momentum transfer allows the use of the non-relativistic formula. The non-relativistic formula is

$$\frac{d^2\sigma}{d\omega' d\Omega} = \frac{r_0^2 m_e \omega'}{2\omega\left|\vec{k}-\vec{k}'\right|}\overline{X}(\theta)J(p_z) \qquad (7)$$

where

$$\overline{X}(\vartheta) = \left(\frac{\omega'}{\omega}+\frac{\omega}{\omega'}-\sin^2\theta\right), \text{and}$$

$\left|\vec{k}-\vec{k}'\right|, J(p_z)$ are defined above with

θ : scattering angle.

This non-relativistic formula is now very similar to the Klein-Nishina formulation for Compton scatter. Indeed, only the inclusion of the

momentum vector terms and the atomic Compton profile of the specific atom mark the difference between the two formulations. The similarity to the Klein-Nashina formula is used in the double scatter development to represent the non-relativistic form of the impulse approximation as the Klein-Nishina formula with a correction factor—the Compton profiles.

Finally, the non-relativistic impulse approximation with polarization effects included is

$$\frac{d^2\sigma}{d\omega' d\Omega} = \frac{r_0^2 m_e \omega'}{2\omega\left|\vec{k}-\vec{k}'\right|}\overline{X}(\xi)J(p_z) \qquad (8)$$

where

$$\overline{X}(\xi) = \left(\frac{\omega'}{\omega} + \frac{\omega}{\omega'} - 2\cos^2\xi\right),$$

ξ : angle between ε and direction of scatter,

ε : electric vector of incident photon,

$\left|\vec{k}-\vec{k}'\right|, J(p_z)$ are defined above.

In this work, the single Compton scatter will be approximated with Equation (7). The doubly differential cross section will be used to calculate the angular dependence of the single scatter spectrum. And, the polarized formulation was shown because the format will be used both in a comparison to Rayleigh scattering and for the double scattering. Finally, the Klein-Nishina equation was included both for completeness and because further developments of the code presented in Chapter 3 will make use of the non-Doppler broadened calculations.

Rayleigh Scatter

Unlike Compton scatter, Rayleigh scatter does not transfer any energy to the electron in the scatter process. Consequently, the scattered photon has the same energy as the incident photon. This leads to several simplifications in the theory and calculation of the Rayleigh scattered photon.

To begin, since the final energy is the same as the initial energy, Rayleigh scatter does not have a corollary to the Compton scatter formula for calculating the final energy. Secondly, for Rayleigh scatters, the polarization remains unchanged. Thus, a photon whose polarization is known would retain the same polarization following a Rayleigh scatter. Similarly, the lack of polarization of the source gamma rays means that Rayleigh scatter does not result in any polarization of the source photons.

There are several other fundamental differences between Rayleigh and Compton scatter. At 100 keV, the Rayleigh cross section is sharply forward peaked for scatter within aluminum [Evans, 1955]. At this energy, approximately 60% to 70% of the Rayleigh scatters are confined to the forward 15 degrees [Evans, 1955]. The Rayleigh scatter cross section for unpolarized radiation is

$$\frac{d\sigma_{RS}}{d\Omega} = \frac{r_0^2}{2}\left(1+\cos^2\theta\right)F(Z,\theta) \qquad (9)$$

where

$F(Z,\theta)$: free atom form factor

Z: atomic number of scattering material

θ : angle between incident and scattered photon.

Figure 5 shows the value of the free atomic form factor for aluminum versus different Q values. Q is simply a parameter that depends on the photon energy and on the angle of scatter. The equation for determining the value of Q in the form factor is

$$Q = 2\left(\frac{\omega'}{m_e c^2}\right)\sin\left(\frac{\theta}{2}\right). \qquad (10)$$

A scattering angle of 90 degrees gives a calculated Q value of about 5 and a corresponding form factor of approximately 0.3 for an 88.03 keV photon in aluminum (See Figure 5). At 45 degrees scattering angles Q equals 2.7 giving a value of approximately 1.2 for the form factor. Since the cross section for scatter is proportional to the form factor, a 90 degree scatter is less likely to occur than a 45 degree scatter since the form factor is smaller.

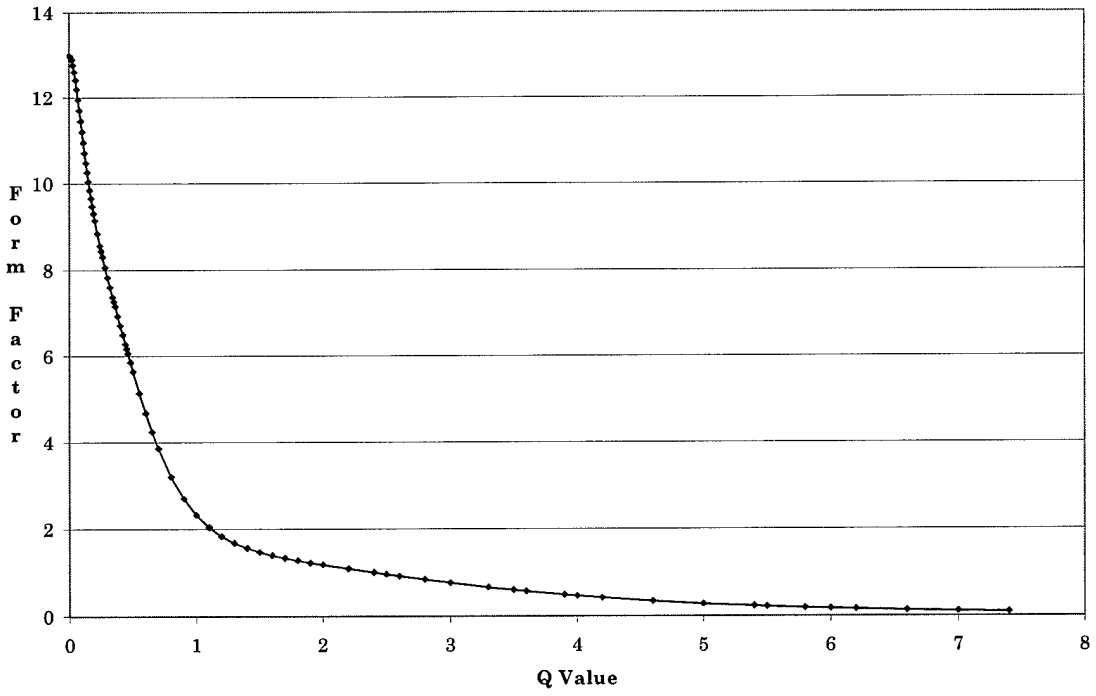

Figure 5: Free Atom Form Factor for Aluminum [Data from Schaupp, 1983]

Similar in form to equation (10), but also utilizing the polarization of the incident photon, the Rayleigh scatter cross section for polarized radiation is

$$\frac{d\sigma_{RS}}{d\Omega} = r_0^2 F(Z,\theta)\sin^2\xi \qquad (11)$$

where

$F(Z,\theta)$: free atom form factor,

Z: atomic number of scattering material,

θ: angle between incident and scattered photon,

ξ: angle between incident electric vectors and scattered direction.

Rayleigh scatter is approximately 5~7% of the total scatter cross section for gamma rays in the energy range of interest. Thus, including the effects of Rayleigh scatter is necessary to properly characterizing both single and the double scatter spectra.

Section 2.2: Double Scatter Physics

In this section, the physics of the different types single scatter shall be combined together to describe the mechanism of double scatter. The correlation between the two scatters is simply the partial polarization resulting from a Compton scatter. Thus, if polarization is disregarded, it is sufficient to simply multiply the cross sections of two single, non-polarized scatter events together in order to obtain the double scatter cross section. If,

however, polarization is included, then it is necessary to develop new equations to deal with the correlation between the two scatters.

In the case of double scatter, then, there are four separate permutations to consider between the Rayleigh or Compton scatters. The first type of scatter is Compton-Compton scatter. This double Compton scatter sequence must account for the partial polarization of the photon following the first scatter to accurately describe the physics. The Compton-Rayleigh scatter also experiences a partial polarization because the Compton scatter results in the partial polarization which affects the Rayleigh scatter cross section. Finally, the Rayleigh-Rayleigh scatters and the Rayleigh-Compton scatters do not need to account for the polarization since no partial polarization occurs before the second scatter.

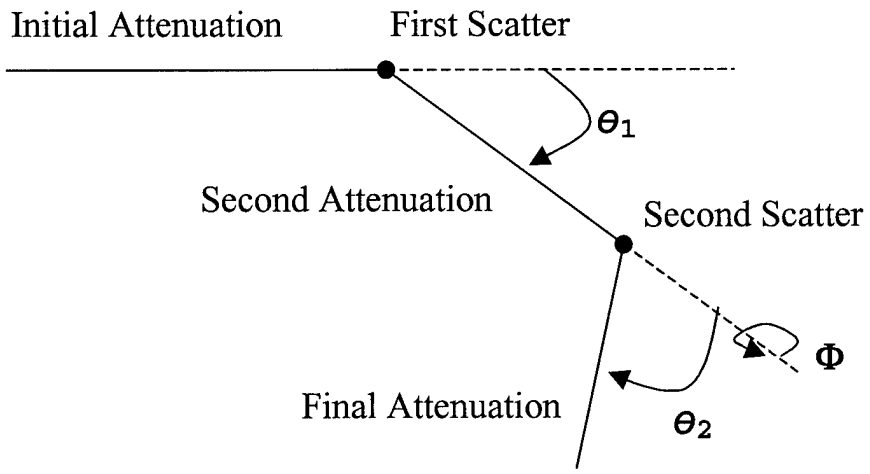

Figure 6: Double Scatter Geometry

The double scatter geometry shown in Figure 6 has several geometrical definitions. The first scattering angle, θ_1, is the angle between the incident

photon and the first scattered photon. These two directions of the photons can be considered to define two vectors. The two vectors, then, define a plane of interaction. In a similar manner, the angle, θ_2, represents the angle between the first scattered photon and the second scattered photon. These two photons also form a plane of interaction. The angle Φ represents the angle between these two planes.

Compton-Compton Scatter

Klein and Nishina, following their derivation of the single scatter formula, studied the Compton-Compton double scatter. Their work was continued by Wightman in 1948 when the Compton double scatter formula was fully derived in order to account for photons which enter the sample non-polarized, experience partial polarization, and finally exit the sample to strike a detector which does not detect polarization [Wightman, 1948]. Thus, the model accounts for the partial polarization of a non-polarized source through a double scatter to a standard energy detector.

If polarization is not included in the model, it is sufficient to simply apply the Klein-Nishina equation twice. If Doppler broadening is required, apply impulse approximation equation twice in succession. Yet, if polarization is required and Doppler broadening is not required, then Wightman's equation is needed to describe the series of scatters [Wightman,

1955]. The non-Doppler broadened, Compton-Compton double scatter equation is

$$\frac{d^2\sigma_{DS}}{d\Omega_1 d\Omega_2} = \frac{r_0^4}{4}\left(\frac{\omega''}{\omega}\right)^2 \left(\gamma_{01}\gamma_{12} - \gamma_{01}\sin^2\theta_2 - \gamma_{12}\sin^2\theta_1 + \right. \qquad (12)$$
$$\left. +2\sin^2\theta_1 \sin^2\theta_2 \cos^2\Phi\right)$$

where

θ_1 : angle between incident and 1st scattered photon,

θ_2 : angle between incident and 2nd scattered photon,

ω: energy of incident photon,

ω': energy of 1st scattered photon,

ω'': energy of 2nd scattered photon,

$$\gamma_{01} = \frac{\omega'}{\omega} + \frac{\omega}{\omega'},$$

$$\gamma_{12} = \frac{\omega''}{\omega'} + \frac{\omega'}{\omega''}.$$

When the effects of polarization and Doppler broadening are required, it is necessary to modify equation (12). The equation is modified by equation (7) in which it was assumed that the impulse approximation only adds the Compton profile factor and the photon momentum terms [Halonen, 1979]. Thus, the Doppler broadened, double Compton scatter equation is

$$\frac{d^4\sigma_{DS}}{d\omega' d\Omega_1 d\omega'' d\Omega_2} = \frac{r_0^4}{4}\frac{m_e^2}{\left|\vec{k}-\vec{k}'\right|\left|\vec{k}'-\vec{k}''\right|}\left(\frac{\omega''}{\omega}\right)^2\left(\gamma_{01}\gamma_{12} - \gamma_{01}\sin^2\theta_2 - \gamma_{12}\sin^2\theta_1 + 2\sin^2\theta_1\sin^2\theta_2\cos^2\Phi\right)J(p_{z1})J(p_{z2}) \quad (13)$$

where

$$\left|\vec{k}-\vec{k}'\right| = \left[\omega^2 + (\omega')^2 - 2\omega\omega'\cos\theta_1\right]^{1/2},$$

$$\left|\vec{k}'-\vec{k}''\right| = \left[(\omega')^2 + (\omega'')^2 - 2\omega'\omega''\cos\theta_2\right]^{1/2},$$

$$p_{z1} = \frac{\left[\omega\omega'(1-\cos\theta_1) - m(\omega-\omega')\right]}{\left|\vec{k}-\vec{k}'\right|},$$

$$p_{z2} = \frac{\left[\omega'\omega''(1-\cos\theta_2) - m(\omega'-\omega'')\right]}{\left|\vec{k}'-\vec{k}''\right|},$$

$J(p_{z1})$ & $J(p_{z2})$: experimentally found Compton profiles.

Having developed the equation for Compton-Compton double scatter with polarization and Doppler broadening, it is instructive to note that the equation for double scatter with polarization is simply a squaring of the single scatter equation with an additional term—namely the $\cos^2\Phi$ term. This term gives an azimuthal dependence to the double scatter cross section. In particular, note that the $\cos^2\Phi$ term is a value between 0 and 1. Thus, the new, polarization-included formula is always less than or equal to the squaring of the non-polarized Klein-Nishina formula because the only added term is the $\cos^2\Phi$ term.

Compton-Rayleigh Double Scatter

Having handled the Compton-Compton double scatter cross section, the next important reaction is the Compton-Rayleigh double scatter cross

section. The Compton-Rayleigh cross section includes the effects of polarization because of the partial polarization of the photons following the Compton scatter. To develop the Compton-Rayleigh double scatter formula, the Klein-Nishina formula is examined first. The Klein-Nashina formula reduces to a type of elastic scattering called Thompson scattering [Evans, 1955]. It occurs as a limiting case for the Klein-Nishina formula when the energy transfer is very small. Yet, the Rayleigh cross section is calculated for the case when there is no energy transfer. As a result, Rayleigh scattering is simply Thompson scattering times the atomic form factor discussed in the Rayleigh section above [Evans, 1955]. To show this development, the Thompson scattering formula is compared to the Klein-Nashina formula. The development is

to start with the Klein - Nashina formula as

$$\frac{d\sigma_{CS}}{d\Omega} = \frac{r_0^2}{2}\left(\frac{\omega'}{\omega}\right)^2\left(\frac{\omega'}{\omega} + \frac{\omega}{\omega'} - 2\cos^2\xi\right). \qquad (14)$$

If the limiting case where ω' is equal to ω,
then the Thompson formula is found as

$$\frac{d\sigma_{TS}}{d\Omega} = r_0^2 \sin^2\xi .$$

Yet, this equation is nearly identical to the equation for single Rayleigh scatter. Thus, I propose the use of a modified form of either equation (13) for Doppler broadening or equation (12) for no Doppler broadening for the Compton-Rayleigh double scatter. These equations were developed for the double Compton scatter case. The new Compton-Rayleigh equations are

$$\frac{d^2\sigma_{DS}}{d\Omega_1 d\Omega_2} = \frac{r_0^4}{4}\left(\frac{\omega'}{\omega}\right)^2 \left(\gamma_{01}\gamma_{12} - \gamma_{01}\sin^2\theta_2 - \gamma_{12}\sin^2\theta_1 + \right. \qquad (15)$$
$$\left. +2\sin^2\theta_1 \sin^2\theta_2 \cos^2\Phi\right) F(Z,\theta_2)$$

where

θ_1 : angle between incident and 1st scattered ihoton,

θ_2 : angle between incident and 2nd scattered photon,

ω : energy of incident photon,

ω' : energy of 1st scattered photon,

$$\gamma_{01} = \frac{\omega'}{\omega} + \frac{\omega}{\omega'},$$

$$\gamma_{12} = 2,$$

$F(Z,\theta_2)$: free atom form factor.

The Doppler broadened formula for the Compton-Rayleigh double scatter is

$$\frac{d^3\sigma_{DS}}{d\omega' d\Omega_1 d\Omega_2} = \frac{r_0^4}{4}\frac{m_e}{\left|\vec{k}-\vec{k}'\right|}\left(\frac{\omega'}{\omega}\right)^2 \left(\gamma_{01}\gamma_{12} - \gamma_{01}\sin^2\theta_2 - \gamma_{12}\sin^2\theta_1 + \right. \qquad (16)$$
$$\left. +2\sin^2\theta_1 \sin^2\theta_2 \cos^2\Phi\right) J(p_{z1}) F(Z,\theta_2)$$

where

$$\left|\vec{k}-\vec{k}'\right| = \left[\omega^2 + (\omega')^2 - 2\omega\omega'\cos\theta_1\right]^{1/2},$$

$$p_{z1} = \frac{\left[\omega\omega'(1-\cos\theta_1) - m(\omega-\omega')\right]}{\left|\vec{k}-\vec{k}'\right|},$$

$J(p_{z1})$: experimentally found Compton profiles,

$F(Z,\theta_2)$: free atom form factor.

The above equations now define the Compton-Rayleigh scatter series. These equations are necessary in order to define the case in which polarization is necessary. The non-polarized case can be represented by a simple multiplication of the Rayleigh scatter formula, equation (9), with the Klein-Nishina formula, equation (3).

Rayleigh-Compton Double Scatter

For Rayleigh-Compton scatter, use the appropriate series of equations depending upon whether Doppler broadening is needed. For non-Doppler broadened scatters, use the Rayleigh scatter formula, equation (9), multiplied by the Klein-Nishina formula, equation (3). For the Doppler broadened case, use the Rayleigh scatter formula, equation (9), multiplied by the impulse approximation for non-polarized photons, equation (7).

Rayleigh-Rayleigh Double Scatter

For the case in which a photon double scatters via Rayleigh followed by another Rayleigh scatter, use the Rayliegh scatter formula, equation (9), twice.

Summary of Double Scatter Physics

In this chapter, the angularly dependent cross sections for single and double scatter have been developed for photons of energy less than 100 keV. The Compton inelastic scatter formula was developed. And, the Rayleigh elastic scatter formula was developed. For the Compton scatter, the assumption of no momentum of the electron for the Klein-Nishina formula was removed by introducing the theory of the impulse approximation. The

polarization between the two scattering events has been examined for the double scatter case. Finally, the physics of all of these events have been combined in order to give the angularly dependent, double scatter cross section for four different cases: Compton-Compton, Compton-Rayleigh, Rayleigh-Compton, and Rayleigh-Rayleigh.

Chapter 3: Development of Computer Code

The newly developed deterministic code calculates the energy spectrum from single and double scatter components. This code, called MOCADS, uses a Monte Carlo integration routine to calculate the single and double scatter components.

Section 3.1: Overview of Double Scatter Deterministic Code

The double scatter, deterministic code was developed using a Monte Carlo integration scheme. Monte Carlo integration is summarized concisely in Numerical Methods [Press, 1992]. A simple example of Monte Carlo integration is finding the area of a circle. Although this example has an exact solution, it is worth while to examine the Monte Carlo integration's basic concepts. To begin, inscribe the circle in a square. Next, choose a point randomly in the square and determine whether the point falls in the inscribed circle. As many points are chosen, the area of the circle can be determined by multiplying the area of the square times the ratio of the points in the circle to the total points chosen in the square.

Indeed, this method can be used to integrate any function over an interval. The function need only be expressed in terms of its dependent variable over the interval. Although the function may not be integrable analytically, it can still be integrated numerically. An advantage of the

Monte Carlo method of integration is that it can easily be extended to multiple dimensions. Another advantage of the Monte Carlo method is that it converges at a faster rate than other numerical methods for higher order multiple integrals. Since, the function of interest in this problem is a six or eight dimensional integral, it is particularly important that the method chosen integrate the function efficiently over multiple dimensions.

Since this code has been developed specifically for this effort, it is important to examine both the implementations of the physics and the algorithm. The implementation of the physics portion leads to the multiple dimensional integral mentioned above. The section describing the algorithm examines in detail how the program handles the integral.

Section 3.2: Implementation of Physics

The goal of the program is to produce an energy spectrum of the double scatter component of the signal. In order to calculate the energy spectrum, a probability spectrum will instead be calculated. This probability spectrum is intended to show the probability that a photon incident on the sample will result in a count in a particular energy bin. Thus, the output is the likelihood that the outgoing photon will undergo two scatters resulting in a particular energy.

Although several steps in the calculation are similar to Monte Carlo transport calculations, this deterministic method is not a transport method.

Indeed, other deterministic codes exist which perform transport. Yet, this code is not intended to substitute for any type of transport code. As an example, this code cannot distinguish where and how much energy was deposited in the sample because the photons incident on the sample are not conserved. MOCADS is designed only to give the specific output of the shape and magnitude of the output energy spectrum versus energy given that a photon is incident on the sample from the source.

To create the deterministic code, a series of physical events is simulated. To begin, the probability that a photon reaches the site of the first scatter is calculated. Next, the probability that the scatter occurs is found. This is followed by another calculation that the photon reaches the site of the second scatter, the probability of the second scatter occurring, and finally the probability that the photon exits the sample. In essence, this is a series of attenuation calculations interspersed with two scatter probability calculations.

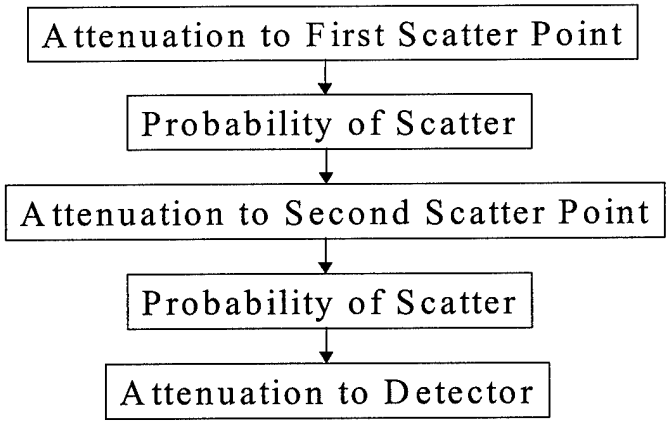

Figure 7: Physical Process of Double Scatter

The equation for the probability of the particle traveling a particular distance in some material is [Turner, 1995]

$$\frac{I(d)}{I_o} = e^{-\mu d} \qquad (17)$$

where

I_0 : incident photon intensity,

d : distance photon travels in medium,

μ : total photon linear attenuation coefficient.

The probability of a particular angular scatter arises from the angularly dependent cross sections discussed in Chapter 2. The simple case when polarization is not needed uses a calculation of a probability distribution function. The distribution function is calculated by integrating the cross section over all angles and energies in the case of Doppler broadening. The cross section is then evaluated at the specific angle needed to carry the photon to the next scatter location or the final destination of the detector. Finally, the angularly dependent cross section is divided by the total cross section just calculated above. The formula to find the probability of scatter through a particular angle is [Adapted from Duderstadt, 1979]

$$p_s(\omega',\theta)=\frac{\sigma_s(\omega\rightarrow\omega',\theta)}{\int\sigma_s(\omega\rightarrow\omega',\Omega)d\Omega} \qquad (18)$$

where

p_s : probability of scatter,

ω' : scatter energy of photon,

ω : incident energy of photon,

θ : scatter angle of photon,

Ω : solid angle,

σ_s : scatter cross section (either Rayleigh or Compton).

If the polarization is included, the formulation uses the same principle except that the total scatter probability must now be integrated over both solid angles. Thus, the double scatter must be evaluated for both scatter angles and their respective solid angle distributions. The new equation is

$$p_{ds}(\omega',\omega'',\theta_1,\theta_2)=\frac{\sigma_{ds}(\omega\rightarrow\omega',\omega'\rightarrow\omega'',\theta_1,\theta_2)}{\iint\sigma_{ds}(\omega\rightarrow\omega',\omega'\rightarrow\omega'',\theta_1,\theta_2)d\Omega_1 d\Omega_2} \qquad (19)$$

where

p_{ds} : probability of double scatter,

ω : incident energy of photon,

ω' : 1st scattered energy of photon,

ω'' : 2nd scattered energy of photon,

θ_1 : 1st scattered angle of photon,

θ_2 : 2nd scattered angle of photon,

Ω_1 : solid angle after 2nd scatter,

Ω_2 : solid angle after 1st scatter,

σ_{ds} : double scatter cross section.

The probability calculation above does not consider the attenuation between the two scatter points. Yet, the attenuation does not change any of the variables in the calculation. Instead, the attenuation term only reduces the probability that a photon reaches the second scatter location. Thus, it

suffices to include the term following the calculation of the scattering probability. Mathematically, the calculation of the probability of scatter is separable from the calculation of the probability of the photon reaching the scatter point.

The effects of $1/r^2$ dispersion of the photon took some care in order to avoid the blow up of the term at or near zero. The total integral was spit into two separate integrals—one integrating over all scatter points outside some small radius. The other integral evaluated over scatter points inside that same small radius. For the purposes of the MOCADS calculation, the second integral was assumed to be negligible in comparison to the integrand over the points outside the small radius. This radius was chosen by the user in order to drive the inner integral towards zero while keeping the outer integral managable by the Monte Carlo integration technique. To keep the integral manageable, it is necessary that the variance of the outer integral be kept low. This corresponds to a larger radius. Thus, some tradeoff was necessary. For the MOCADS simulations presented, a small radius of 1 mm was chosen as the best tradeoff.

Section 3.3: Algorithm of the Deterministic Code

This code was designed to allow the user to disable certain features such as the Doppler-broadening effect, polarization, and single scatter calculations. In the algorithm that follows, however, it is assumed that all

features are included in order to show the full scale of the algorithm without completely overwhelming the details of the code. A wire frame diagram of the code showing the various options is presented in Figure 8.

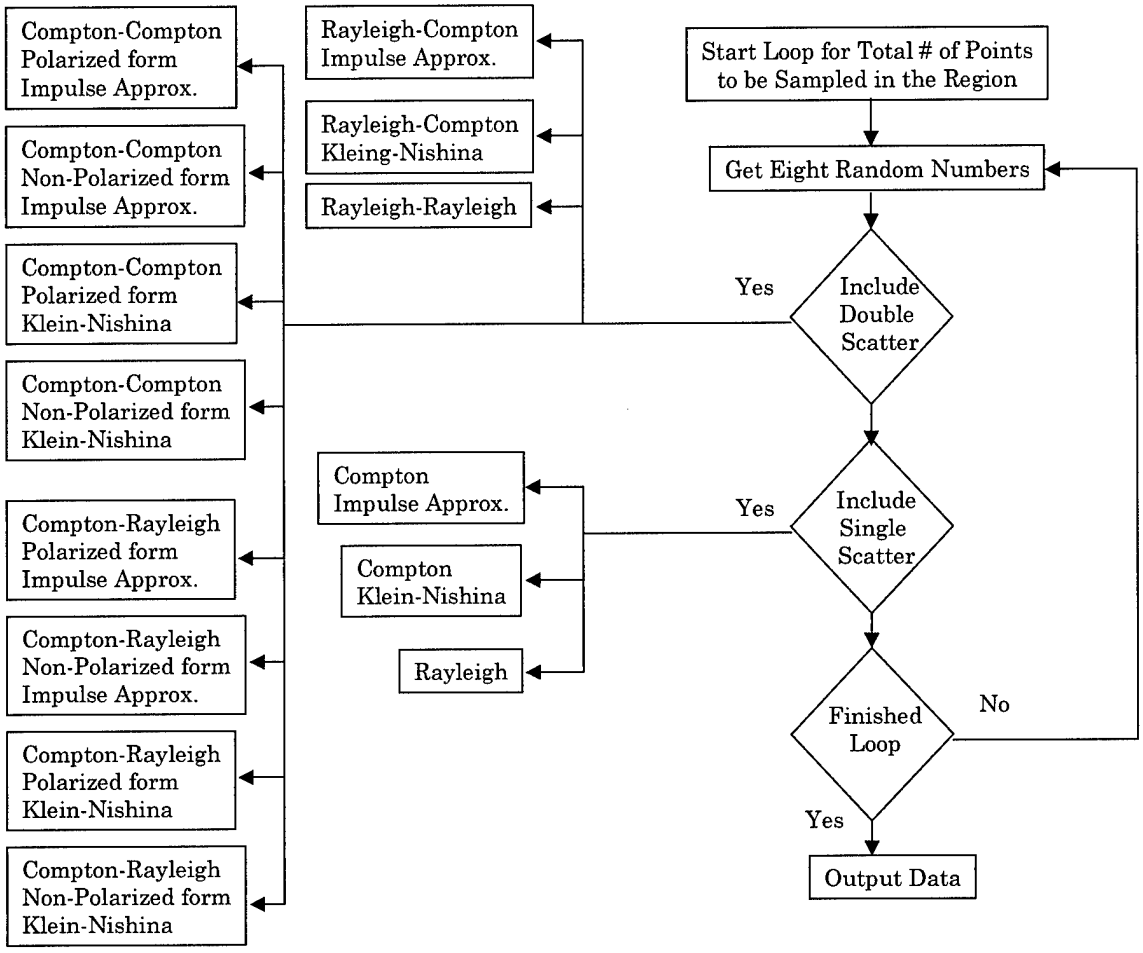

Figure 8: Wire Frame Diagram Showing Code Options

To begin, the code reads in the user-directed inputs from a source file. Then, having the total number of points needed provided by the user, the code enters a loop to determine the relative probabilities. Eight random numbers determine the (x, y, z) coordinates of the two scatter points and the intermediate and final energies of the photon. Following the location

determination, the program checks to ensure that the points lie in sensible positions. Thus it checks to make sure that the positions are not in the corrosion region and that the collimation of the source and detector do not preclude the photon from reaching the particular position.

Once the geometrical calculations are completed, the program then calculates the double scatter spectra and stores each type of scatter series permutation separately. Finally, the program calculates the single scatter spectra using the same random numbers as for the double scatter. Thus, the single scatter and the double scatter calculation for MOCADS are correlated.

Finally, the code exits the loop and begins the last portion of the program. It outputs the spectra as a text file dump of the energy versus probability. The text file is then plotted and viewed in Microsoft Excel.

Chapter 4: Experimental Apparatus and Computer Codes Used for Validation

To validate the deterministic double scatter code developed in chapter 3, a laboratory experiment was performed. The experiment was designed to test the model's prediction of the double scatter spectra. This chapter will explain the design of the experiment and the equipment used to perform the experiment.

In addition to validating the MOCADS code with a laboratory experiment, two computer codes were also used to validate this newly developed code. The first code is a validated code distributed by Los Alamos. This code uses Monte Carlo transport to characterize the energy spectrum. Finally, a deterministic code was developed and validated by AFIT/ENP to calculate the Doppler-broadened, single scatter energy spectrum using a discretized mesh approach.

Section 4.1: Experimental Apparatus

The experimental apparatus is the Multiplexed Compton Scatter Tomograph (MCST). Its major components are the detector arrays, the signal processing equipment, the data collection and display computer software, and the image processing software.

As with any laboratory experiment, the specifications of the MCST are of primary importance if the experiment is to be repeatable. Thus, the following discussion explains the required specifications in order to achieve repeatability of the experiment. The following specifications were provided courtesy of Captain B. Evans and Captain M. Sands.

Detector Arrays

The detector arrays collect photons using high purity germanium (HPGe) crystals within each detector. The total MCST system was designed by Captain B. Evans to image aluminum samples via scattering of Cd-109 gamma rays.

The detection equipment for the MCST is located at AFIT in building 470. The detector array was built by the Princeton Gamma-Tech company located in Princeton, NJ. The device consists of six high purity germanium (HPGe) crystals aligned in a planar geometry. The geometry is shown in Figure 9 and the specifications are given in Table 1.

Table 1: Geometry Specifications for Detector Arrays

Characteristic	Specifications
Active volume	800 mm^3
Active front	80 mm^3
Aperture cover	0.25 mm-thick beryllium foil
Area of aperture cover	78 mm^2
Distance between detectors	1.96 cm

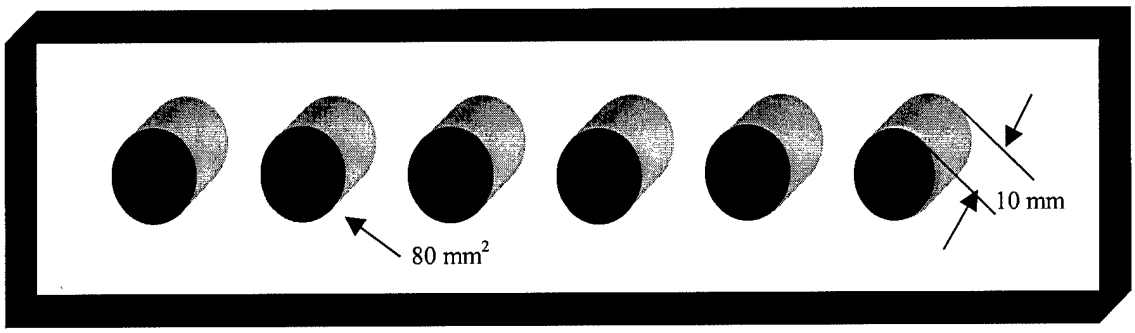

Figure 9: The planar array of identical HPGe detectors, with dimensions of the active volume. The black fronts represent the areas open to incident photons. [Figure provided courtesy of Captain M. Sands]

Aluminum end caps and an aluminum cage are between the HPGe crystals and the beryllium detection windows. The crystals are set back 3.5 mm from the window. The arrangement causes a field of view limitation of approximately 40 degrees off of the normal to the detector crystal. Unfortunately, the distance between the beryllium shield and the set back crystals limit the array such that only four detectors can be used to view the sample. However, the signal in the actual experiment was so low that this particular limitation was not an issue since only two crystals actually received any distinguishable signal.

The detectors have a voltage bias of positive 1500 volts which was provided by an ORTECT #659 Bias Supply. The cryostat that houses the detectors is passively cooled by liquid nitrogen. The liquid nitrogen is stored in a dewar which gravity feeds the cryostat.

The energy resolution of the MCST is approximately 433 +/- 100 electron volts (eVs). The resolution of the detector is not accounted for in the

computer model, MOCADS. The energy efficiency is also not accounted for in MOCADS.

Signal Processing System

The signal processing units convert the signal from the detectors into properly shaped pulses that are capable of being recorded by the computer software discussed below. The signal originates in the MCST when a photon enters the HPGe crystal, deposits its full energy within the crystal, and is collected by the internal electronics. The equipment listed in Table 2 processes the signal.

Table 2: Signal Processing Equipment Specifications

Type of Equipment	Model #
Dual Spectroscopy Amplifier	ORTEC #855
Decay Amplifier	ORTEC #427-A
Timing Single Channel Analyzer	ORTEC #552
Gate and Delay Generator	ORTEC #416a
Analog-to-Digital Converter	C.A.E.N. C420
Crate Housing	CAMAC
Crate Controller	Weiner CC166

The signal from the detector travels to the dual spectroscopy amplifier, which provides pole-zero cancellation while shaping and amplifying the pulse. The signal is then split to a delay amplifier and a timing single channel analyzer (T-SCA). The amplifier again amplifies the signal and adds a slight delay so the arrival of the pulse information is coincident with the timing information from the T-SCA. These signals are linked in a gate and

delay generator that positively identifies them and sends the information on to the analog-to-digital converter (ADC). The 8-channel peak detection module receives the analog pulse and accomplishes the conversion, and then sends the digital signal for display.

The ADC is a CAMAC (Computer Automated Measurement and Control) standard. The other units are NIM (Nuclear Instrument Module) standard electronics. A CAMAC crate houses and supplies the power to the modules. The crate controller manages the ADC system providing an interface for the user to control and configure all the modules through a desktop computer. The controller receives start/stop and detector information from the user via the software.

Computer Software

The digital signal passed to the computer was processed through a multi-parameter CAMAC Data Acquisition system (MULTI). MULTI was used to provide experiment control, file management, operation monitoring, archivaling, and graphic display of the data. The data analysis and final display software was completed using Microsoft Excel spreadsheets. The MCST system uses a code developed at AFIT to reconstruct the electron density of the sample object. This research did not reconstruct the electron density; rather, it only examined the shapes of the recorded spectra.

Section 4.2: Experiment

To test the multiple scatter spectra, it was necessary to exclude the single scatter contribution. Excluding the single scatter spectra is quite straightforward since all single scatters must be confined to a plane. Thus, if the detector collimator and the source collimator are not coplanar at any point, then no single scatter photons can enter the detector. In other words, the source collimator and the detector collimator were offset in order to allow only multiply scattered photons into the detector.

To offset the detector and source collimators, a 0.635 cm aluminum plate was placed under the source collimator and the sample. This effected an offset that completely moved the source photons out of the plane of the detector collimator. The sample was located 2.21 cm from the front of the source collimator (see Figure 10). The sample was 1.905 cm wide by 1.905 cm long by 3.175 cm tall.

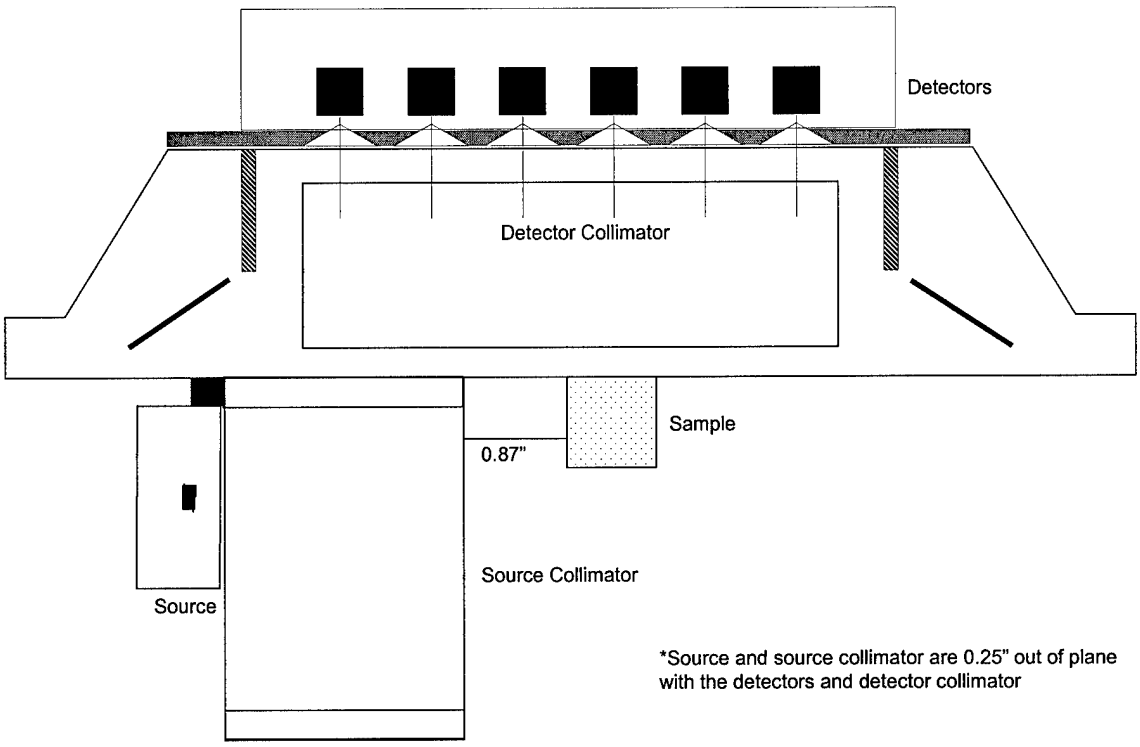

Figure 10: Experiment Geometry

The experiment took roughly 125 hours to complete. A calibration was performed before and after the acquired data sets. The calibration was accomplished by placing a weak Cd-109 source and a weak Am-141 source in front of the detectors. The location of the peak in a particular energy bin recorded by the MCST was noted. A calibration was made by using the known photon energies versus the recorded peak bin.

Section 4.3: Monte Carlo Neutron-Photon Transport Code

The Monte Carlo Neutron-Photon (MCNP) transport code was used to validate the deterministic code described in Chapter 3. The description of the physics and the code's algorithm are available directly from Los Alamos [See

Reference 19]. MCNP is a standard Monte Carlo transport code because it solves the transport equations by using the Monte Carlo method.

The code was expected to be a robust code against which the newly developed deterministic code could be compared. Unfortunately, MCNP was not capable of distinguishing between the different types of scattering processes at the energy range of interest. MCNP does offer an option of removing the coherent scatter portion of the photon cross section. Although this option was examined very closely, the results are not valid in aluminum at an incident energy of 88.03 keV. The key problem with MCNP was the underlying assumption in how the coherent scatter was removed. It was expected that the removal of the coherent scatter would not affect the Compton scatter probabilities. Yet because MCNP removes the coherent scatter portion from the total scatter cross section, the effect of removing coherent scatter was to also reduce the total scatter cross section. The reduction in the total cross section meant that the average photon penetrated farther into the sample and thus over-representing the deeper portions of the sample. This changed the shape of all of the tallied spectra. As a result of the change in the spectra, MCNP could not be used to characterize the underlying shapes of the double scatter spectrum such as the Compton-Compton or the Compton-Rayleigh sub-spectra. These sub-spectra could have been obtained by examining the total spectrum and then subtracting the spectrum in which only Compton scatter was allowed. This limitation

affected the validation MOCADS because any discrepancies between the two could not be resolved by comparing the sub-spectrum. Since the sub-spectra could not be compared, the nature of the discrepancies cannot be directly determined.

Section 4.4: Deterministic Doppler Broadened Single Scatter Code

Captain B. Evans developed a deterministic, Doppler broadened code called Scatgram [Evans, 1997]. The code is fully documented in his doctoral thesis. This code was designed to predict the single scatter spectra for a highly collimated source fan-beam of photons incident on a sample and then detected through a collimator. Physical experiments have validated this code, particularly the Doppler broadened correction to the Compton equation. MOCADS was deliberately developed such that it could also calculate the single scatter spectra. Thus, Scatgram was used to validate the Doppler broadening in the new code.

Chapter 5: Validation of Deterministic Code

The validation of the deterministic code, MOCADS, utilized three separate testing procedures. The first validation test was comparing MOCADS to MCNP. MOCADS was also compared to the results of the laboratory experiment explained in Chapter 4. Finally, the single scatter, Doppler broadened code, explained in Chapter 4, was compared to the single scatter-only portion of MOCADS.

Section 5.1: Validation Using MCNP

The Monte Carlo Neutron-Photon transport code, MCNP, described in chapter 4, was used to validate the multiple scatter calculations performed by MOCADS. The single scatter spectrum without Doppler broadening was verified. The comparisons below show that the single scatter spectrum matches very well. The double scatter comparison between MOCADS and MCNP is shown to be acceptable. Finally, the discrepancies between the two calculations are examined.

MCNP has a few severe limitations with respect to the calculation performed by MOCADS. MCNP does not calculate the partial polarization of the photon following the Compton scatter. Additionally, MCNP does not perform any Doppler broadening of the spectra. Thus, the MOCADS/MCNP

comparison is limited to the case where there is no Doppler broadening and no polarization included in the output spectrum.

In addition to the limited photon physics included in MCNP, it has severe time limitations as well. The calculations for the validation of MOCADS took MCNP nearly 50 hours to complete. In contrast, MOCADS took only three hours. Several factors impact the length of time MCNP requires to calculate a simulation. Most importantly, the geometry of the simulation cannot be efficiently calculated by MCNP. And yet, the type of experiment fixes the geometry into a point source, point detector collection. And, MCNP requires extensive computer run time in the point source, point detector type of arrangement.

Along with the sample geometry limiting MCNP's capabilities, MCNP also contains some unfortunate options with respect to initially starting particles. It allows the user to specify a direction for the starting particle. Also, the user can define a cone around the chosen direction for a region in which the starting particles can emerge. However, the cone must inscribe the sample cube. This leads to the obvious inefficiency of many starting particles having little or no chance of actually interacting with the sample. Thus, MCNP is of limited usefulness as a tool to investigate the multiple scatter spectrum for this thesis due to the lack of several key physical features as well as the extended time period required by each calculation.

In this validation of MOCADS with MCNP, the sample geometry was chosen to accentuate the double scatter spectrum by choosing a large sample with respect to the mean path length of 2.30 cm in aluminum for an 88.03 keV photon. Additionally, in order to obtain the best possible signal, both the detector and the source were left uncollimated. Figure 11 shows the geometry of the MCNP validation. The sample is a 5 cm x 5 cm x 5 cm cube located a distance of 6 cm from the point source. The detectors are aligned 3.5 cm from the sample, spaced 1.0 cm apart. In order to increase the signal, the detectors were chosen as 0.3 cm radius circles rather than point detectors. The detectors are labeled simply 1 to 5 from left to right.

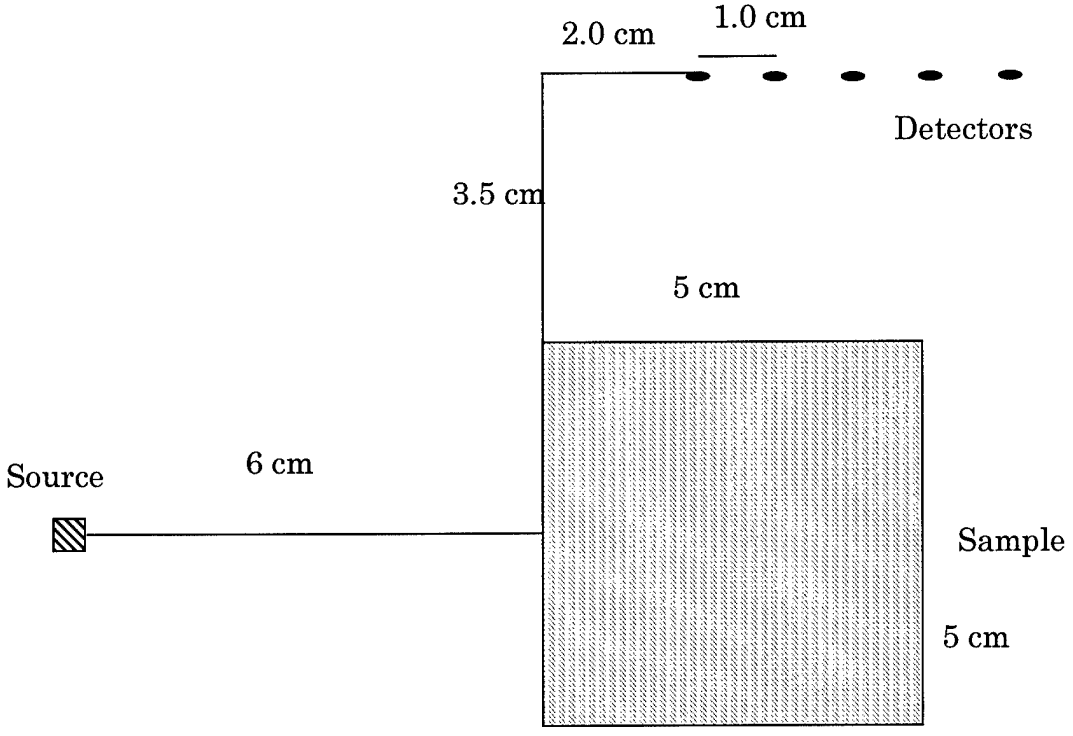

Figure 11: Sample geometry for MCNP validation of MOCADS

The single scatter spectra are shown in Figure 12 through Figure 16. The MCNP spectra are shown with error bars calculated by the code. MOCADS is shown scaled to the maximum of the MCNP spectra for each detector. The MCNP calculation for the peaks at 88.03 keV due to Rayleigh scatter have been omitted from the figure for detectors four and five due to the overwhelming intensity at this energy. The peaks at 88.03 keV were approximately one hundred times larger than the single Compton peaks for those two detectors.

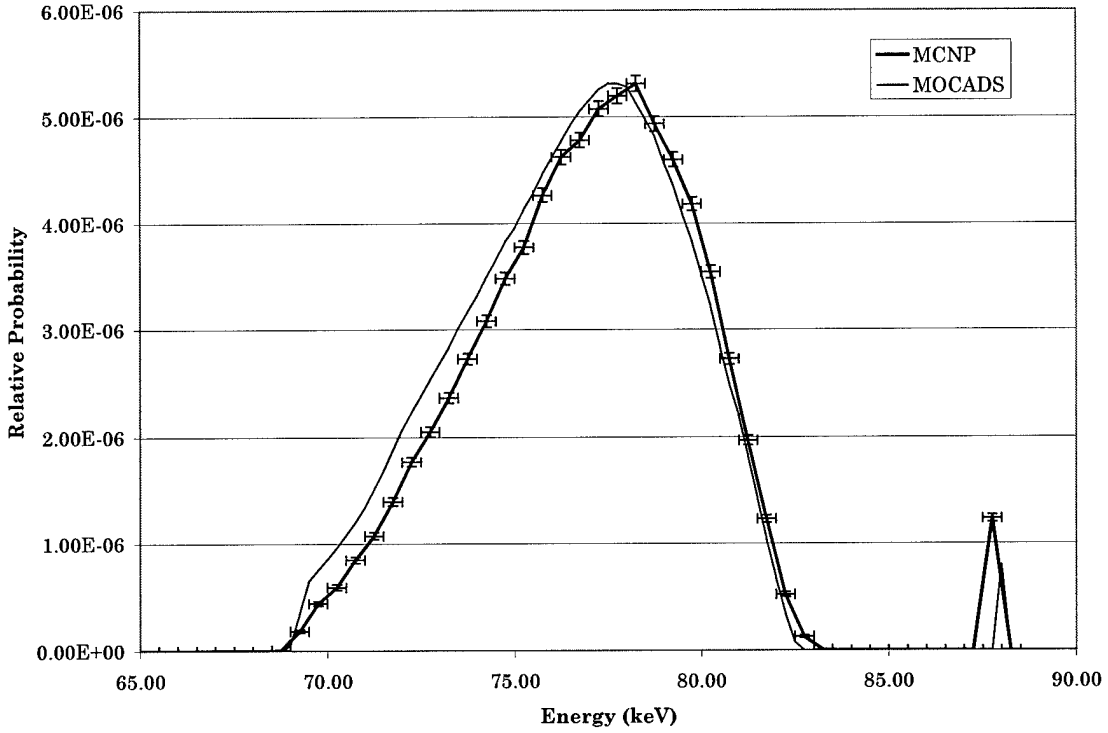

Figure 12: Single Scatter Validation Using MCNP - Detector 1

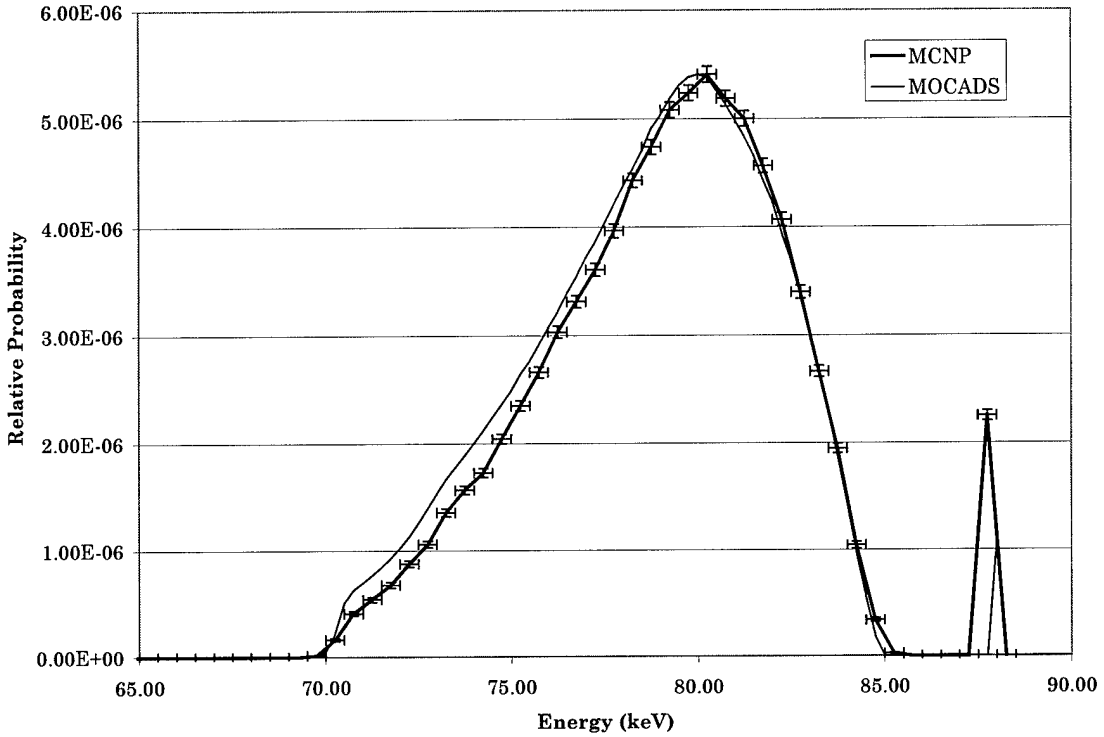

Figure 13: Single Scatter Validation Using MCNP - Detector 2

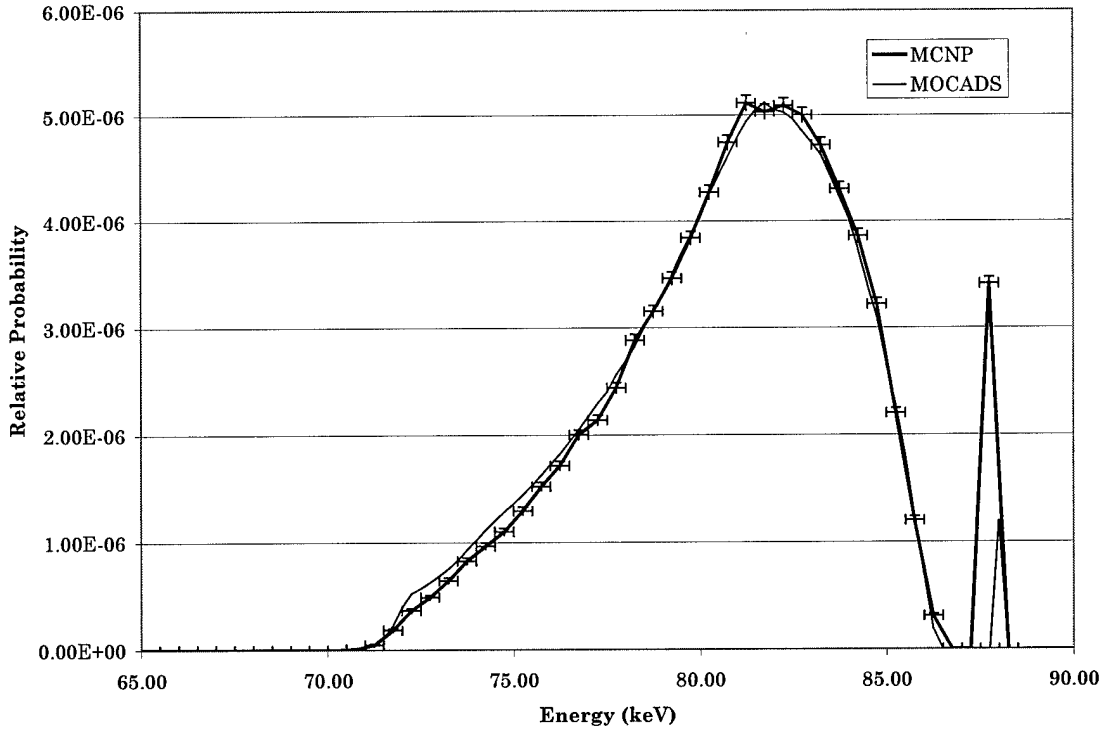

Figure 14: Single Scatter Validation Using MCNP - Detector 3

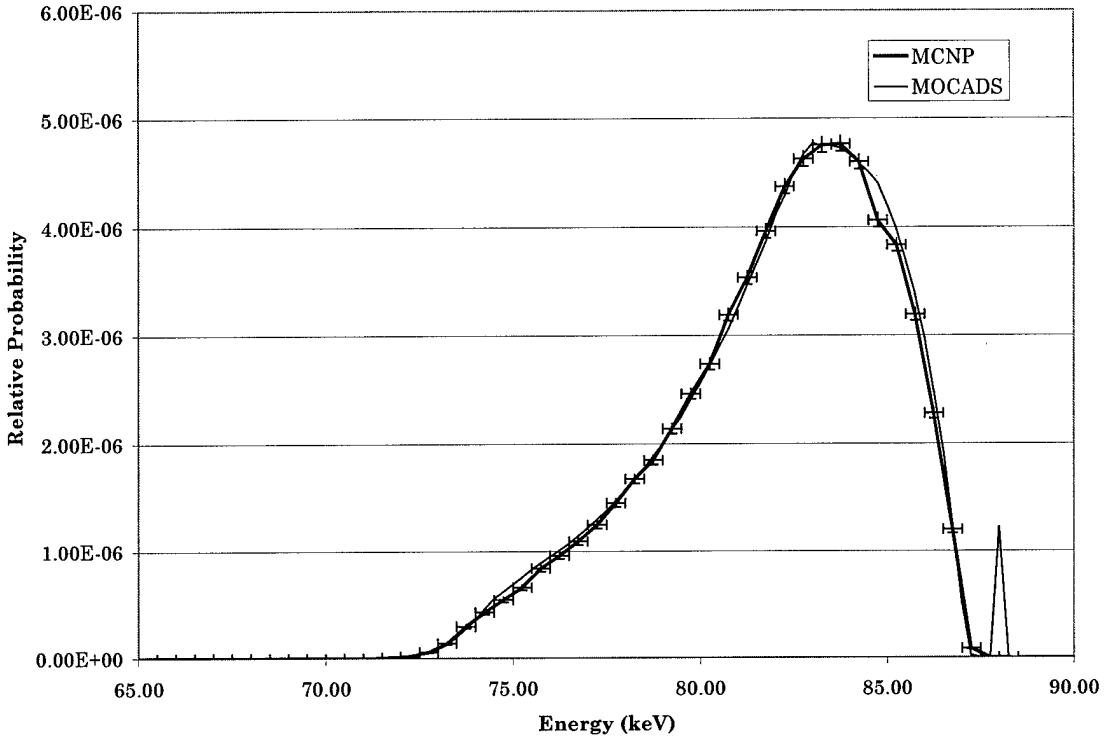

Figure 15: Single Scatter Validation Using MCNP - Detector 4

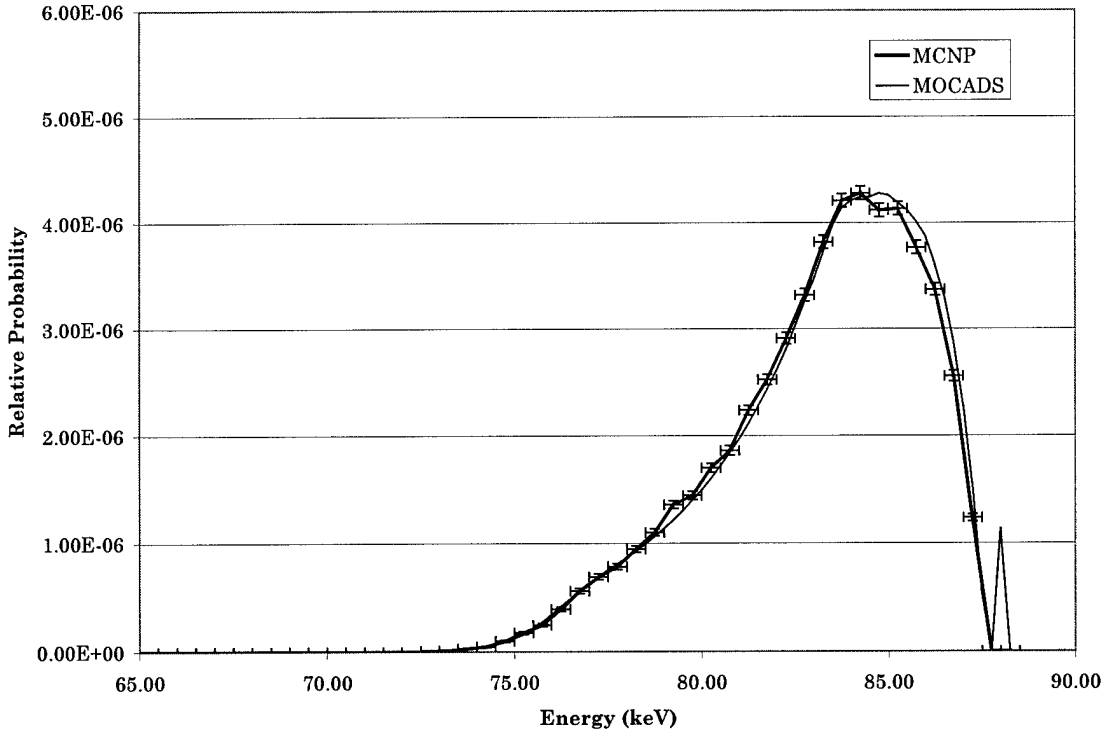

Figure 16: Single Scatter Validation Using MCNP - Detector 5

The comparison shows that MOCADS is accurately calculating the single scatter spectra for all of the detectors. Two problems are shown to exist with MOCADS in this calculation. MCNP predicts 88.03 keV peaks larger than the MOCADS prediction. Additionally, the MOCADS calculations do not lie directly on top of the MCNP calculations. The second problem may, in part, be due to the assumption of the point detector in MOCADS properly characterizing the circular detector in MCNP. To examine this effect, a MOCADS calculation for the single scatter spectra at the leading and far edges of the circular detector was performed. The comparison between MOCADS and MCNP for detector one is shown in Figure 17. The MOCADS calculation bounds the MCNP single scatter calculation showing that the center point is indeed a good approximation to the solid detector.

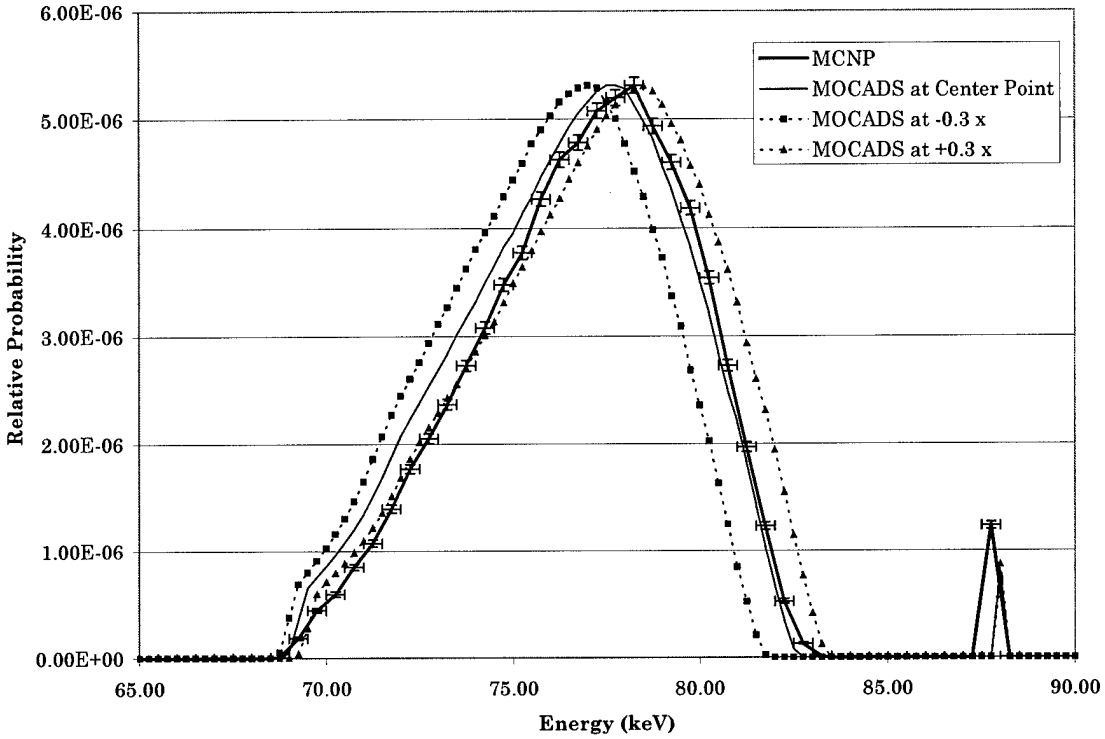

Figure 17: Single Scatter Validation Using MCNP Around Detector 1

The multiple scatter spectra for the five detectors are shown in Figure 18 through Figure 22. The MOCADS output is again scaled to the maximum value for each detector for the MCNP output.

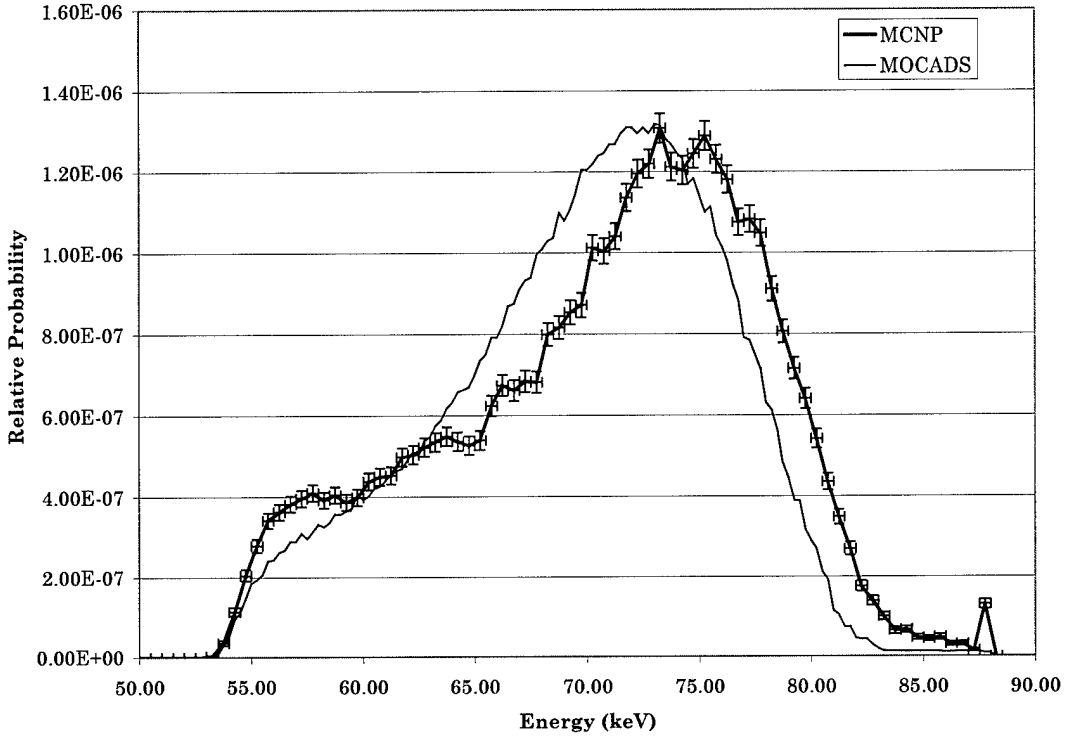

Figure 18: Double Scatter Validation Using MCNP - Detector 1

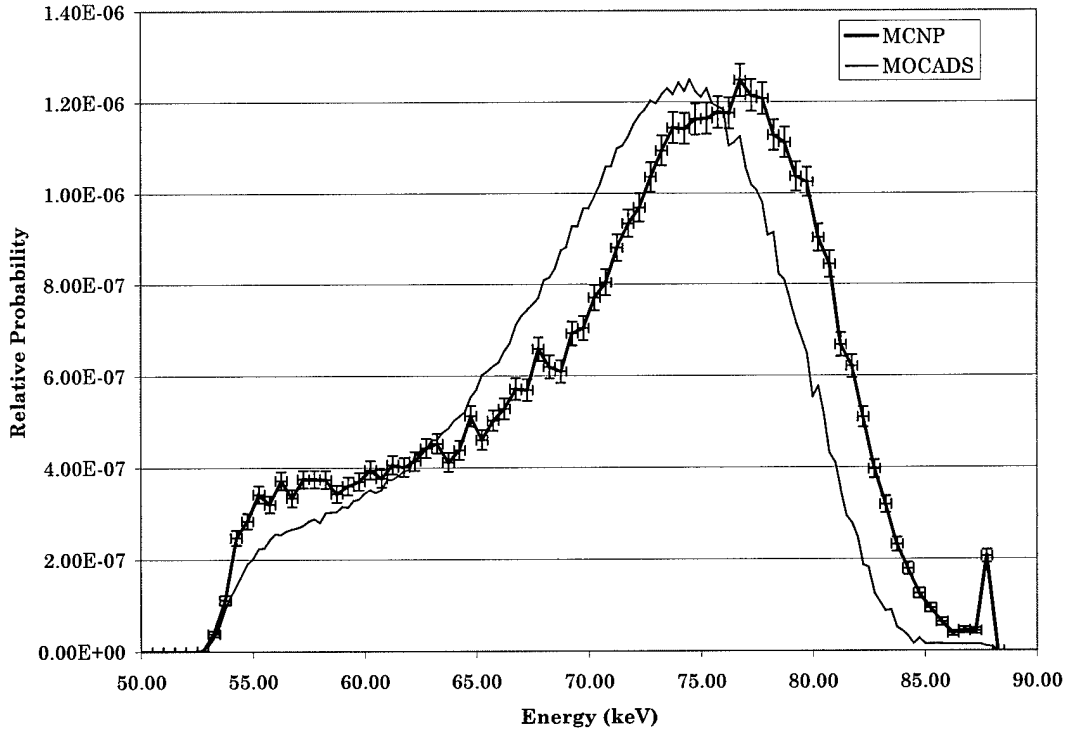

Figure 19: Double Scatter Validation Using MCNP - Detector 2

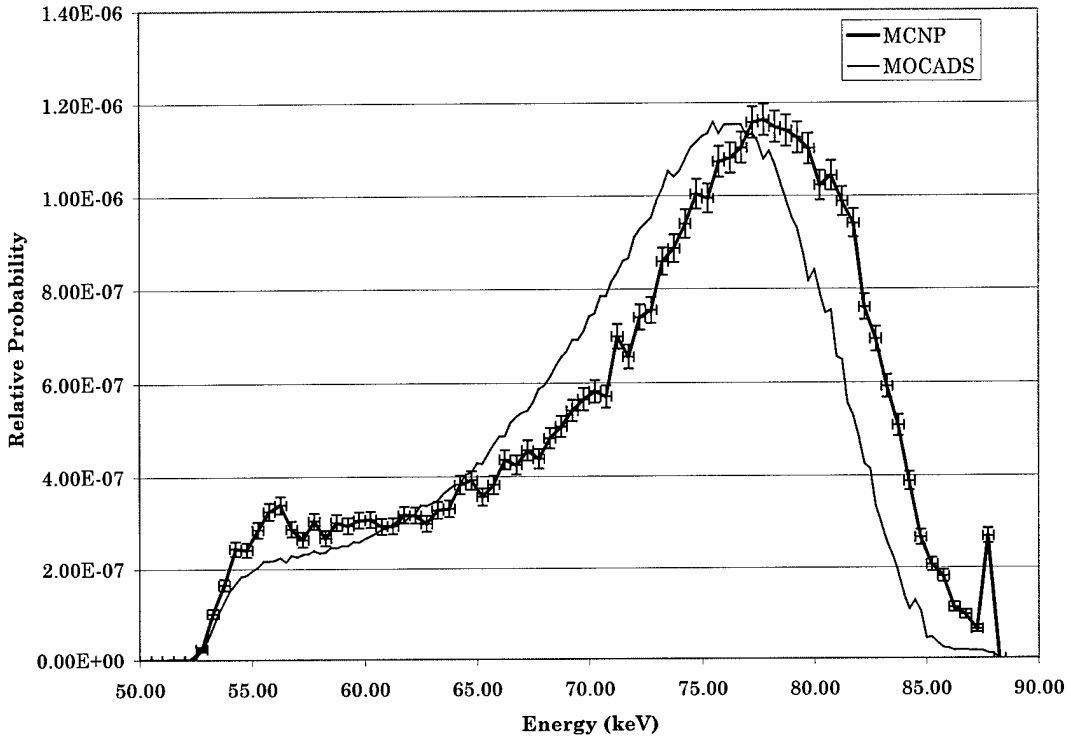

Figure 20: Double Scatter Validation Using MCNP - Detector 3

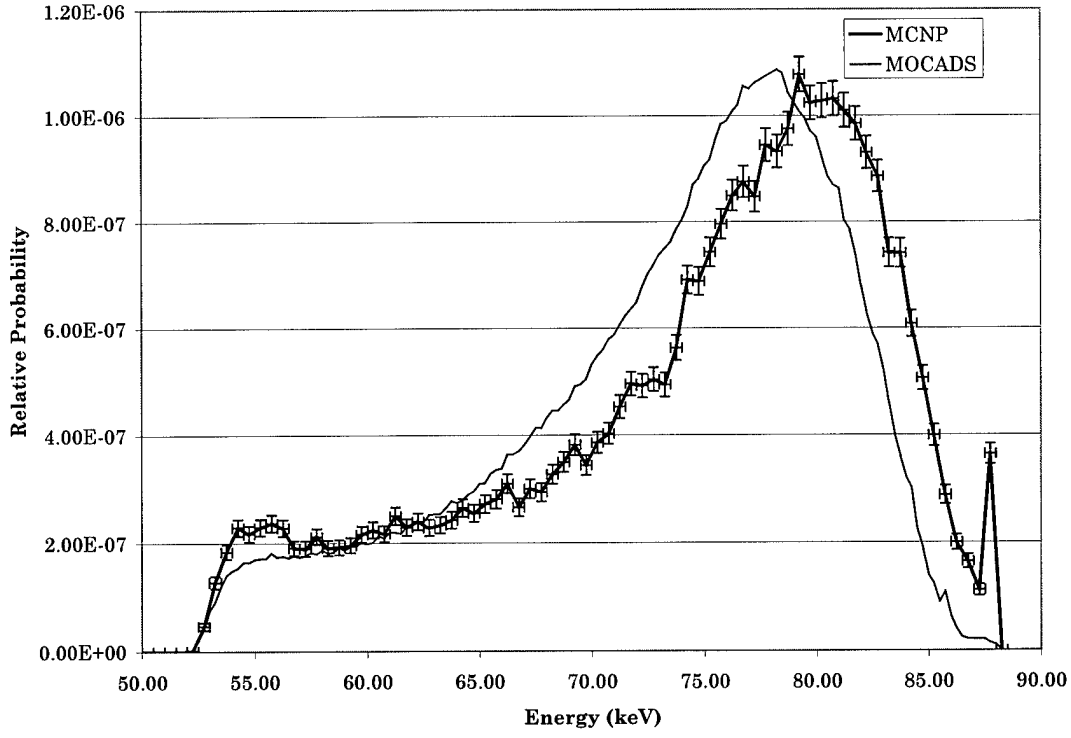

Figure 21: Double Scatter Validation Using MCNP - Detector 4

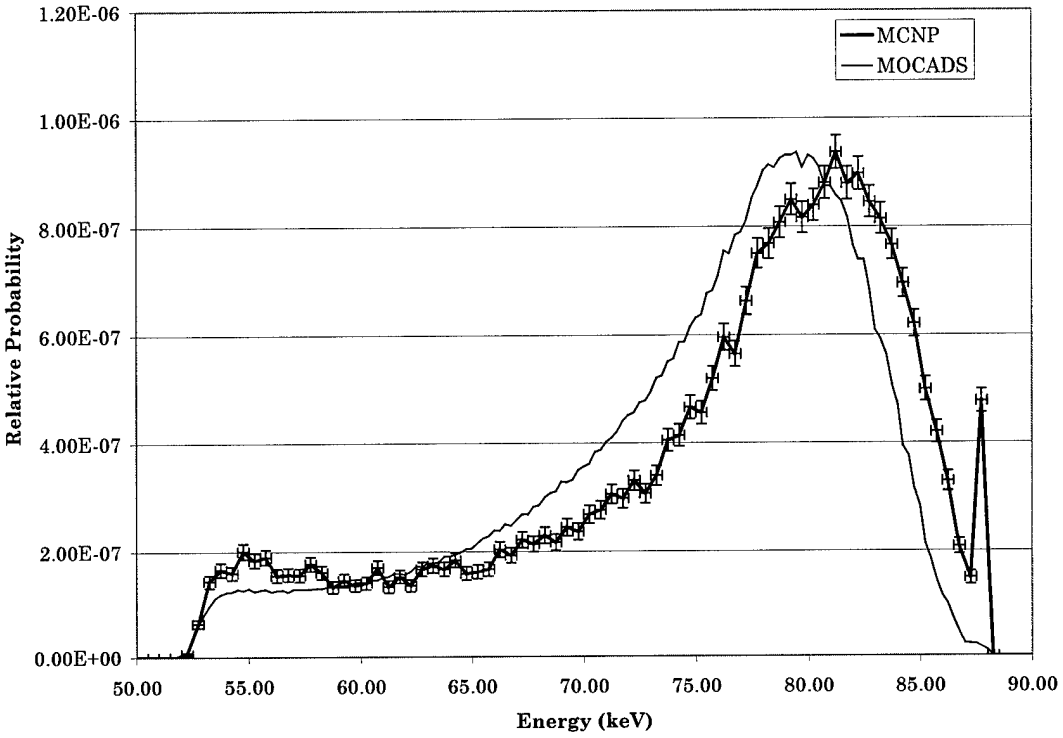

Figure 22: Double Scatter Validation Using MCNP - Detector 5

The MOCADS code predicts the shape of the double scatter spectra accurately. MOCADS is not correctly predicting the 88.03 keV double Rayleigh scatter peak, however. Additionally, the spectra shift on the higher energy side in the MOCADS calculation could be due to the point detector assumption, similar to the errors in the single scatter spectra in Figure 17. A similar double scatter comparison is shown in Figure 23. Here, however, the calculation failed to bound the MCNP-predicted spectrum.

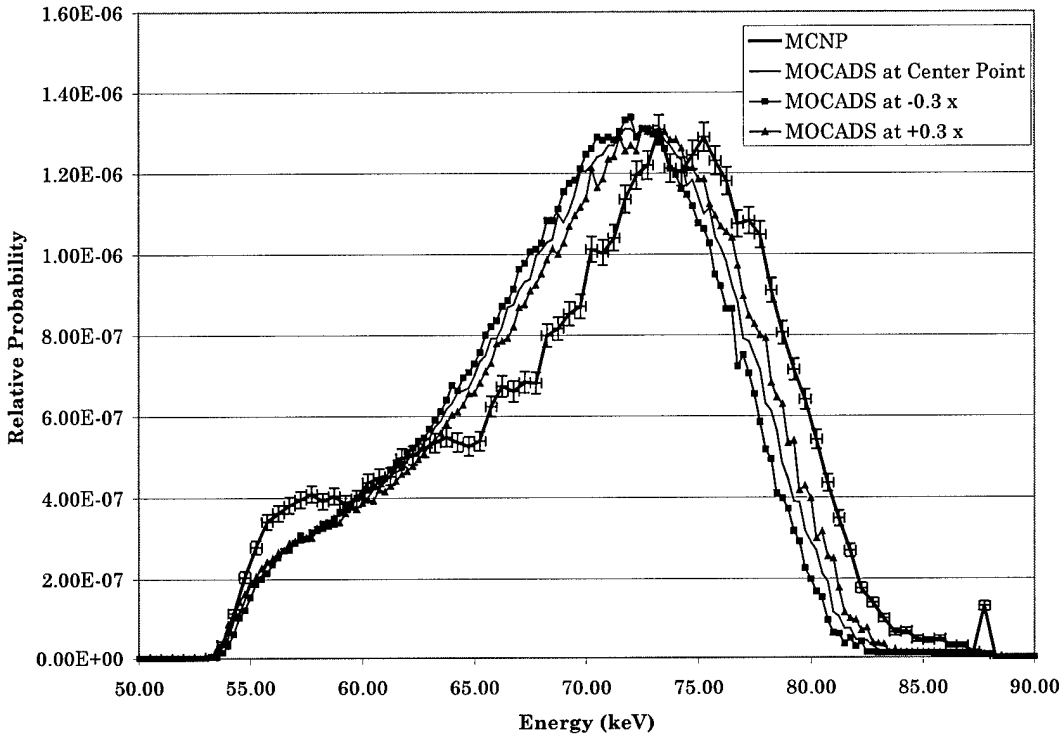

Figure 23: Double Scatter Validation Using MCNP Around Detector 1

The result of this validation is that the MOCADS double scatter is correct, albeit with reservations concerning its predictions about location of the upper edge of the spectrum. MOCADS double scatter spectrum can be considered valid in shape; but, it is not valid for exact determination of the double scatter spectrum. The errors in the Rayleigh scatter components may be significantly contributing to the location of the high energy edge of the MOCADS double scatter spectrum. The MOCADS calculations give a prediction of the correct shape of the double scatter spectrum with respect to the energy dependence, and thus the angular dependence.

A comparison between all the different types of scattering was made using MCNP. The single, double, and higher order scatter spectra were put

on one graph in order to examine the ratios between the three types of scattering. Figure 24 shows that the higher order scatters are important in the regime below the single scatter cutoff. The importance of the higher order scatters is that the double scatter cannot be easily distinguished from the higher order scatters in a laboratory experiment. Also, this figure shows that the assumption that the higher order scatters do not contribute is not wholly valid at the low energy portion.

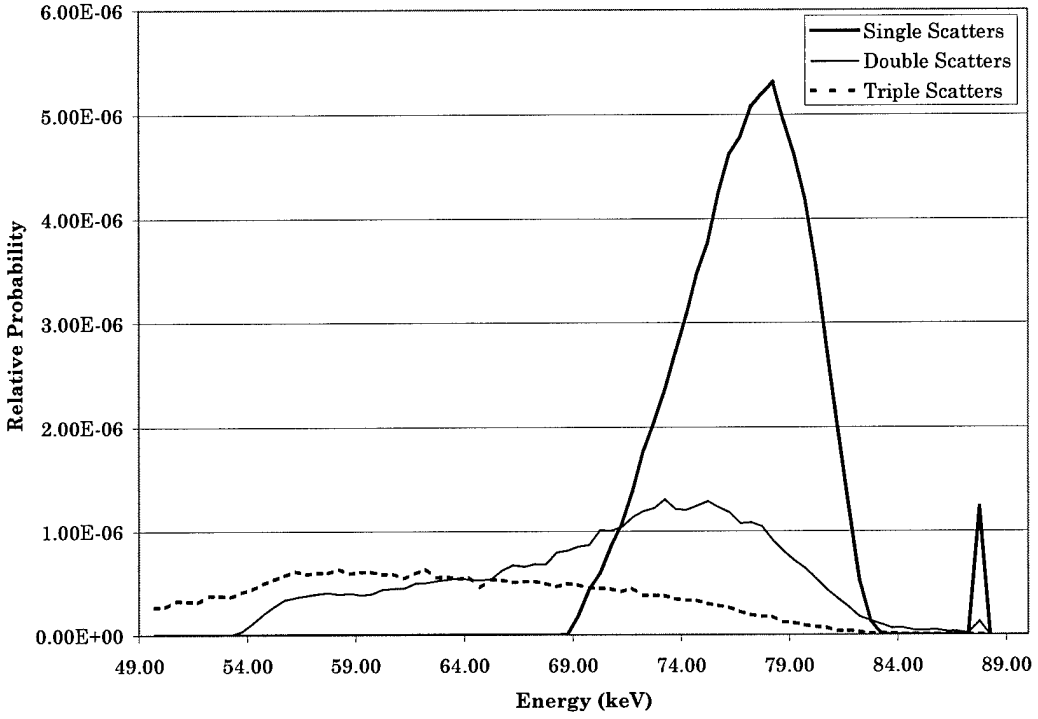

Figure 24: MCNP Comparison for All Scatter for Detector 1

This figure also shows the relative ratios for the single to the double scatter calculated by MCNP. Under the single scatter peak, the double scatter is approximately one-fifth of the single scatter. A similar plot in Figure 25 showing the absolute numbers calculated by MOCADS

demonstrates that MOCADS does not calculate the ratio between single and double scatter properly. Figure 25 is shown on a log-linear scale in order to show both the single and the double scatter.

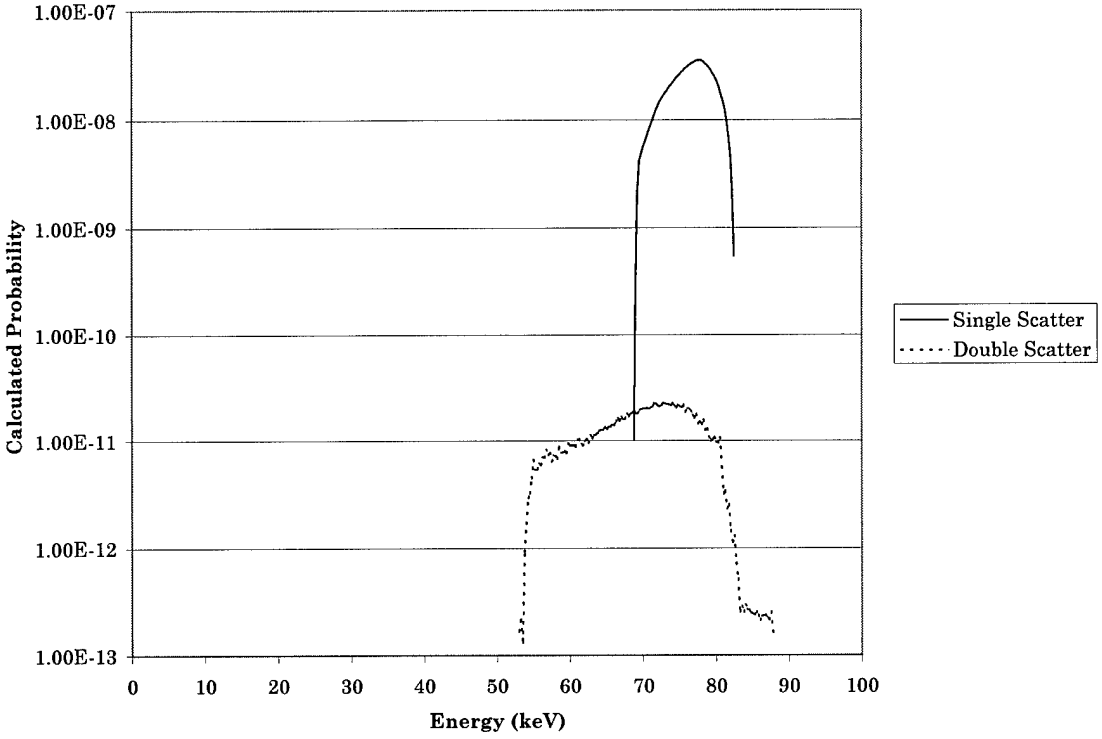

Figure 25: MOCADS Double and Single Scatter Comparison

The comparison between MOCADS and MCNP show that MOCADS calculates the general shapes and the trend of those shapes properly. Yet, the high energy edge of the MOCADS calculations is not the same as the MCNP calculations. Also, the MOCADS calculation does not correctly predict the single to double scatter ratio. This error in the ratio may be due to a loss of proper constants in the calculations. It should be possible to fit a function using MCNP to correct for the incorrect ratios.

Section 5.2: Validation Using the Laboratory Experiment

The experiment was designed to have a multiple scatter spectrum while eliminating any single scatter spectrum. The multiple scatter spectrum was straightforward to obtain; yet, it took a considerable amount of time due to the low probability of the multiple scatter events. The experiment described in Chapter 4 was carried out over 125 hours. Approximately 75 hours were devoted to collecting the signal, and 50 hours to the background. According to Equation (20), this division of 125 hours is nearly optimal when the strength of the signal is nearly the same as the background in intensity. The equation is [Knoll, 1989]

$$\frac{T_{S+B}}{T_S} = \sqrt{\frac{S+B}{B}} \qquad (20)$$

where

T_{S+B} : amount of time for signal + backgound,

T_B : amount of time for just backgound,

S : signal counts,

B : background counts.

If the signal counts are approximately equal to the background counts, then the time spent collecting the signal should be approximately 1.5 times the time spent collecting background.

The setup was described in chapter 4 and its layout is shown in Figure 10. In the experimental setup, the detectors are labeled 1 to 6 from left to right. In this experiment, there was not enough signal in detectors 1, 2, 5, and 6. So, these detectors have been omitted from the calibration results.

The net data for the experiment was very noisy. The data was rebinned for the total signal and the background. The rebinning of the data smoothed it and the results showed a clear pattern. The MCST data has been rebinned such that ten of the original bins are now in one bin. The background was then subtracted from the total signal to give net counts.

The MOCADS calculation was carried out for the two detectors that had sufficient signal to discern a possible shape. The calculation took approximately three hours to complete. The shape of the multiple scatter spectra is clearly similar to the shape predicted by MOCADS. The MOCADS calculation shown includes both the Doppler broadening and the polarization effects. The comparison between the rebinned, experimental data and MOCADS for the two detectors with sufficient signal are shown in Figure 26 and Figure 27. The trend-line shown is a moving average of three of the newly binned data points. The MOCADS output has been scaled to match the detector values.

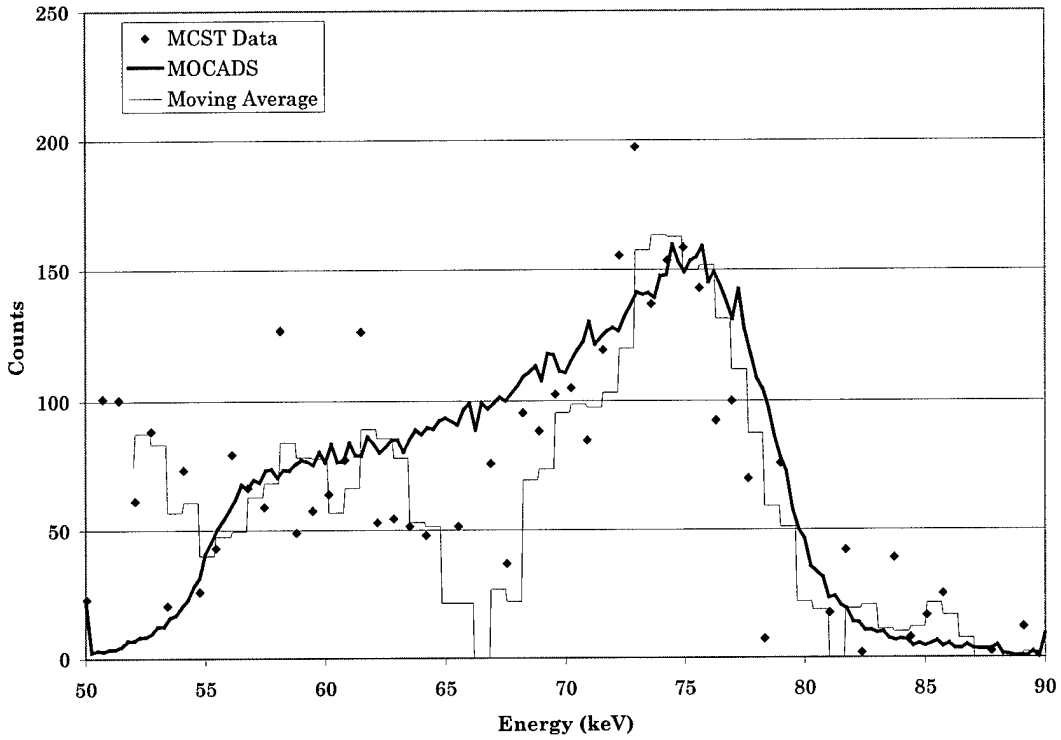

Figure 26: Double Scatter Validation Using Experimental Data – Detector 3

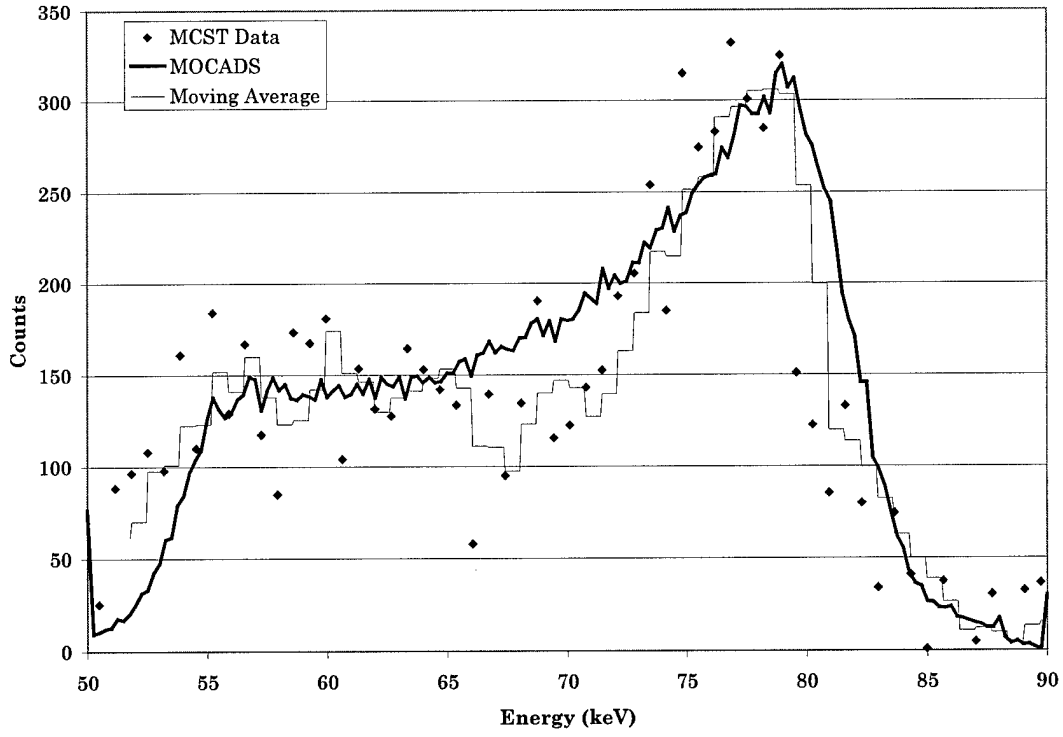

Figure 27: Double Scatter Validation Using Experimental Data – Detector 4

These results show that the MOCADS code is correctly predicting the double scatter spectrum. A difference between the two spectra is apparent in the lower energy tail in the experimental data. This tail is due to the presence of successive scatters beyond twice scattered photons. Although the triple scatters are not as likely as the double scatter, they do contribute to the spectrum significantly below the double scatter cutoff.

The results also show that MOCADS is correctly predicting several key features in the multiple scatter spectra. To begin, the position of the high energy edge of the laboratory data matches nicely in both plots with the MOCADS simulations. Additionally, the laboratory data does not show any significant peak at the double Rayleigh scatter energy of 88.03 keV—in good agreement with the MOCADS simulations.

These findings show that MOCADS is correctly predicting the shape of the double scatter spectrum. And, the findings tend to contradict the comparison performed between MOCADS and MCNP. The MOCADS-laboratory comparison should be stronger indication of the capability of MOCADS to correctly identify the double scatter spectrum accurately. Thus, the apparent discrepancies between MOCADS and MCNP may lie in the modeling performed by MCNP.

Section 5.3: Validation Using the Single Scatter Code

The single scatter, deterministic code described in chapter 4 was used to validate the Doppler-broadened, single scatter calculations performed by MOCADS. The comparison below shows that the output spectra produced are nearly identical from MOCADS to the deterministic code, Scatgram.

Scatgram predicts the single scatter in a plane of interaction. The MOCADS simulation was restricted to a plane for the comparison by creating a sample that was only 1 mm thick. The restriction in MOCADS is reasonable in order to do this limited comparison.

The Scatgram code has been validated extensively with laboratory measurements. Of primary importance to MOCADS, Scatgram has been used to model the Doppler broadening in many single scatter laboratory measurements. The Scatgram comparison, then, can be used directly to validate the MOCADS single scatter code because of the extensive validation.

Scatgram Comparison Without Void

The sample in the Scatgram/MOCADS comparison is 2 cm x 2 cm x 1 mm located a distance of 7.6 cm from the source point. This setup was chosen in an arbitrary manner that primarily focused on ease of use with the Scatgram and MOCADS code. Also, a laboratory experiment was not performed for this design due to time limitations on MCST device. The four

detectors were aligned 1.95 cm apart at a distance of 7.6 cm from the sample. The geometry is shown in Figure 28.

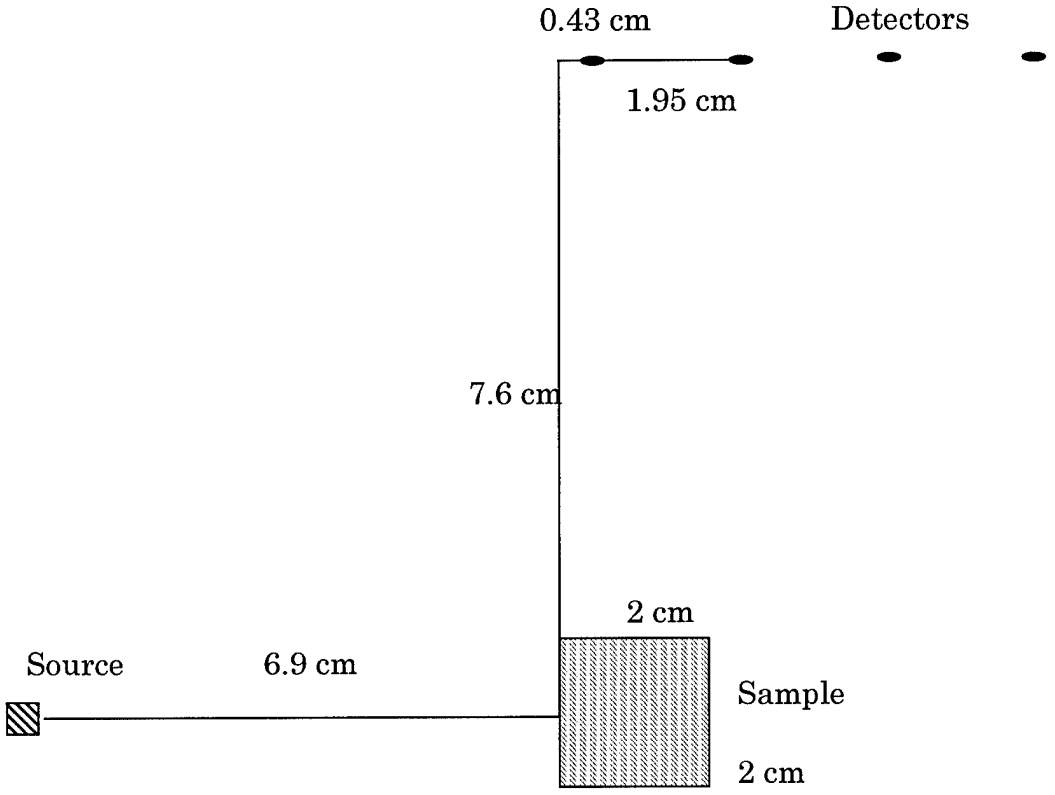

Figure 28: Sample geometry for Scatgram validation of MOCADS

The comparison of MOCADS to Scatgram is shown in Figure 32. The Scatgram figures are scaled such that the maximum of the peak at the first detector is one. The rest of the detectors are scaled using the same scaling factor. The MOCADS Doppler-broadened outputs are scaled directly to the Scatgram calculations. The single scatter, non-Doppler broadened output is included for each detector to demonstrate the amount of Doppler broadening.

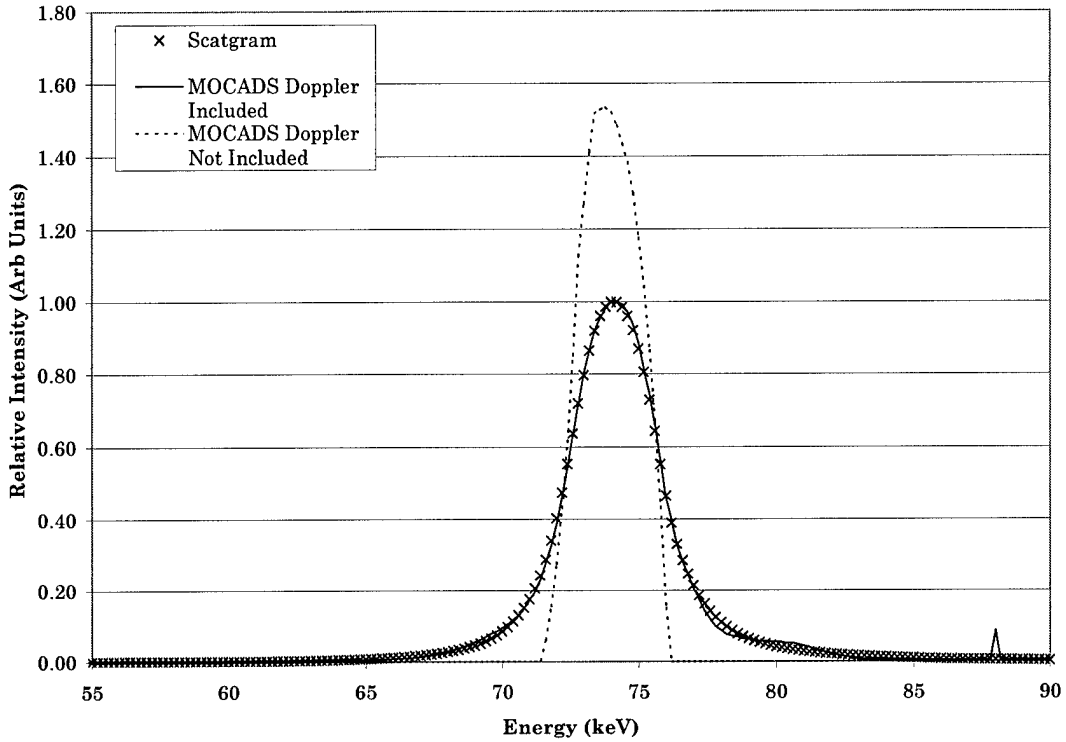

Figure 29: Doppler Broadening Validation Using Scatgram – Detector 1

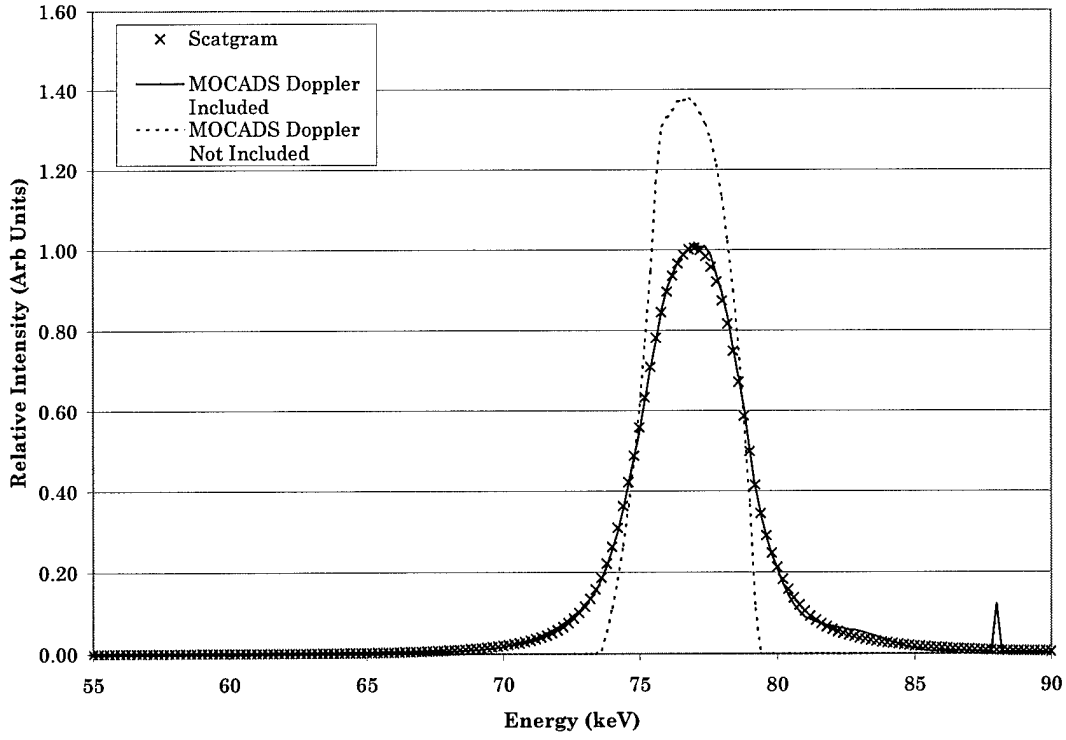

Figure 30: Doppler Broadening Validation Using Scatgram – Detector 2

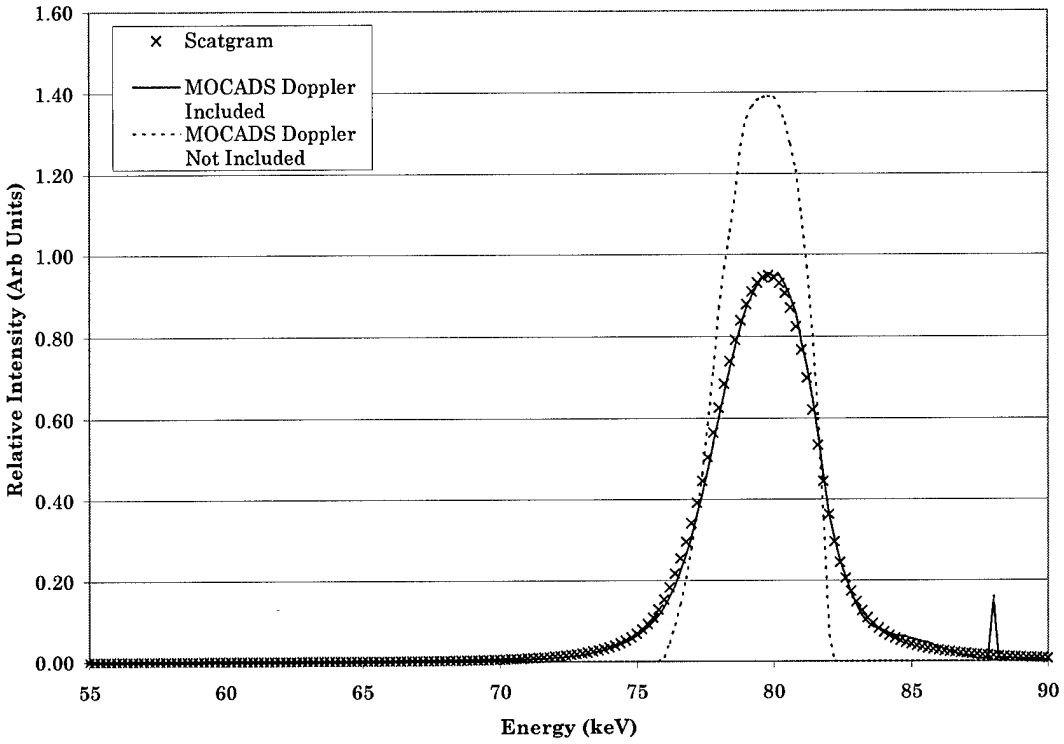

Figure 31: Doppler Broadening Validation Using Scatgram – Detector 3

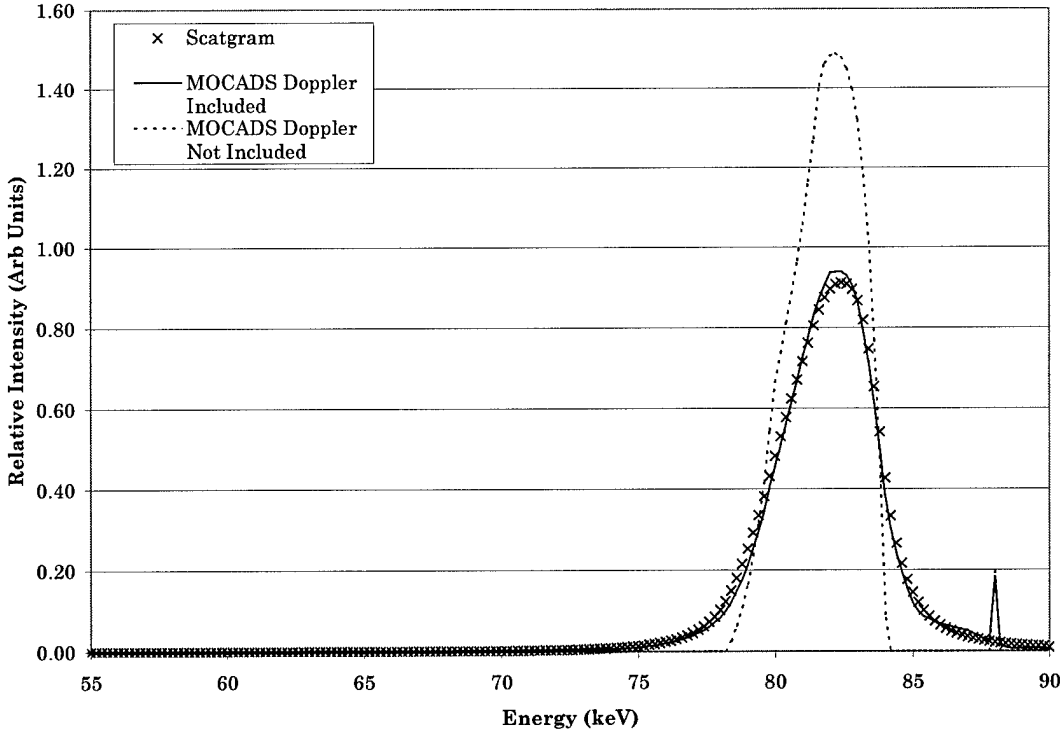

Figure 32: Doppler Broadening Validation Using Scatgram – Detector 4

The Scatgram comparison shows that MOCADS is correctly calculating the Doppler broadening when the sample does not contain a void. The Doppler broadening of double scatter should follow directly since it is a series of single Doppler broadenings.

Scatgram Comparison with Void

A similar geometry was used to determine the effects of a void on the Doppler broadening portion of the code. The change in the geometry from the previous example is that a 1 cm x 1 cm void was place in the center of the sample. The spectra in Figure 33 through Figure 36 were scaled such that the peak for each ouput was one.

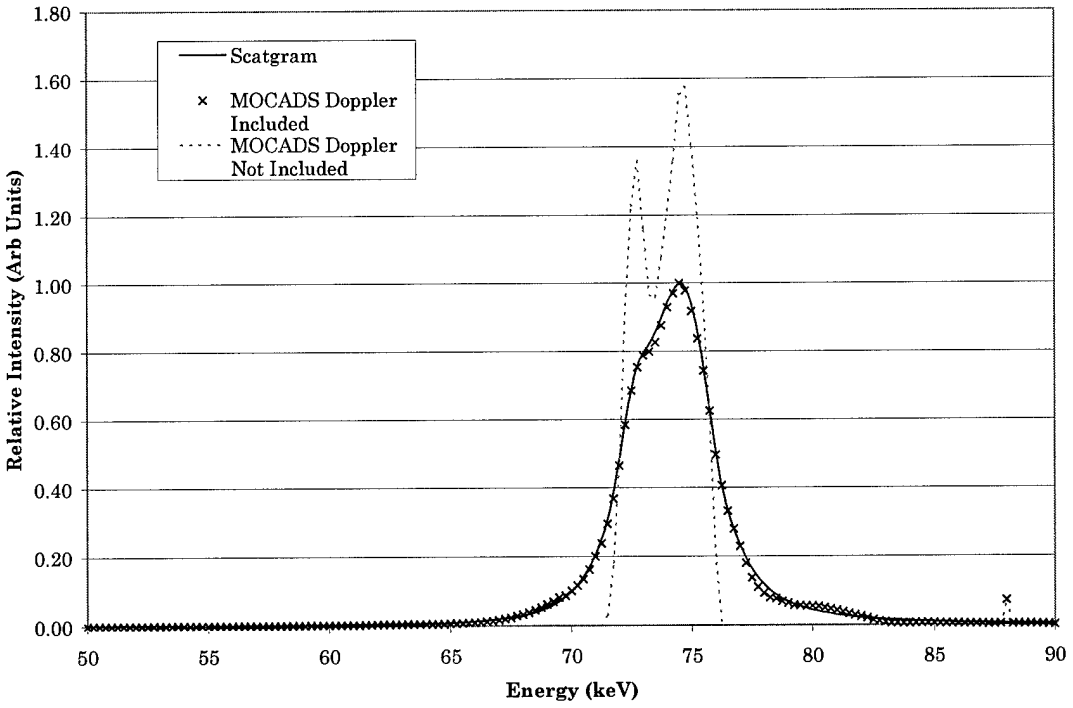

Figure 33: Doppler Broadening when a Void is Included – Detector 1

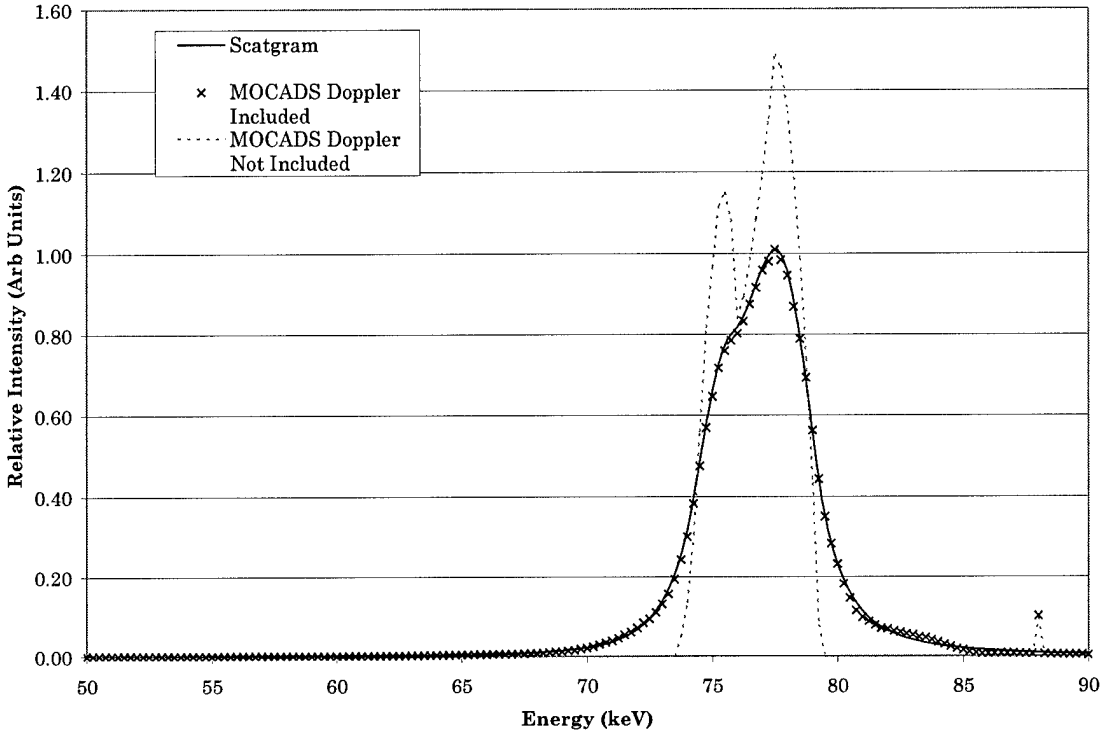

Figure 34: Doppler Broadening when a Void is Included – Detector 2

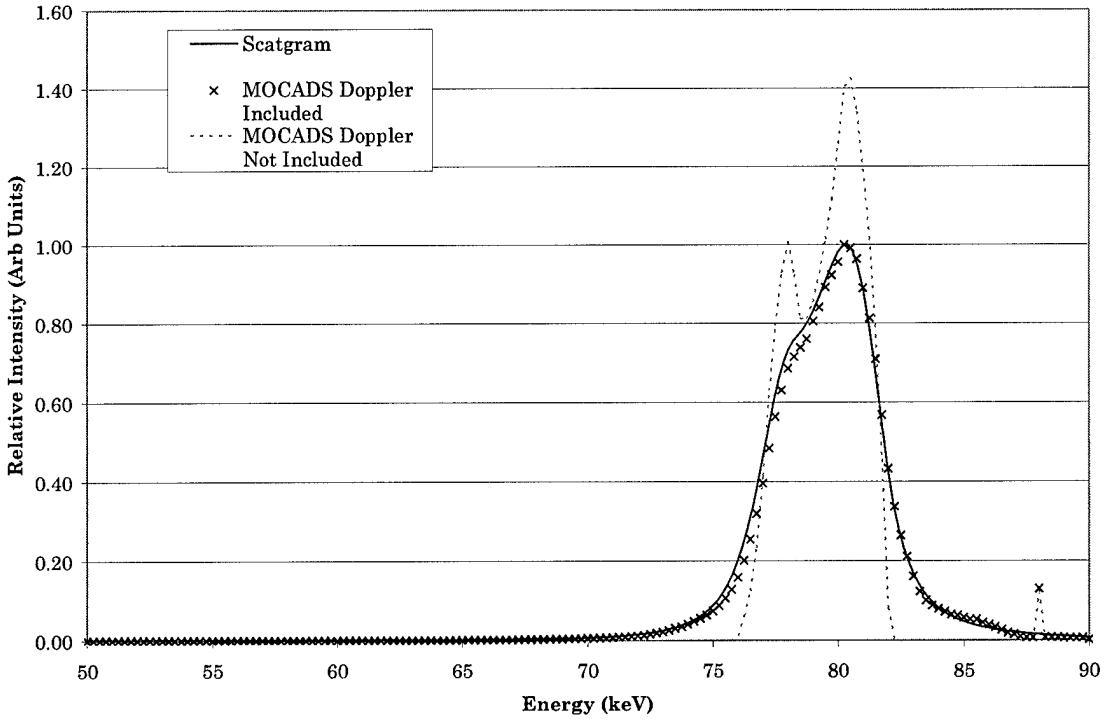

Figure 35: Doppler Broadening when a Void is Included – Detector 3

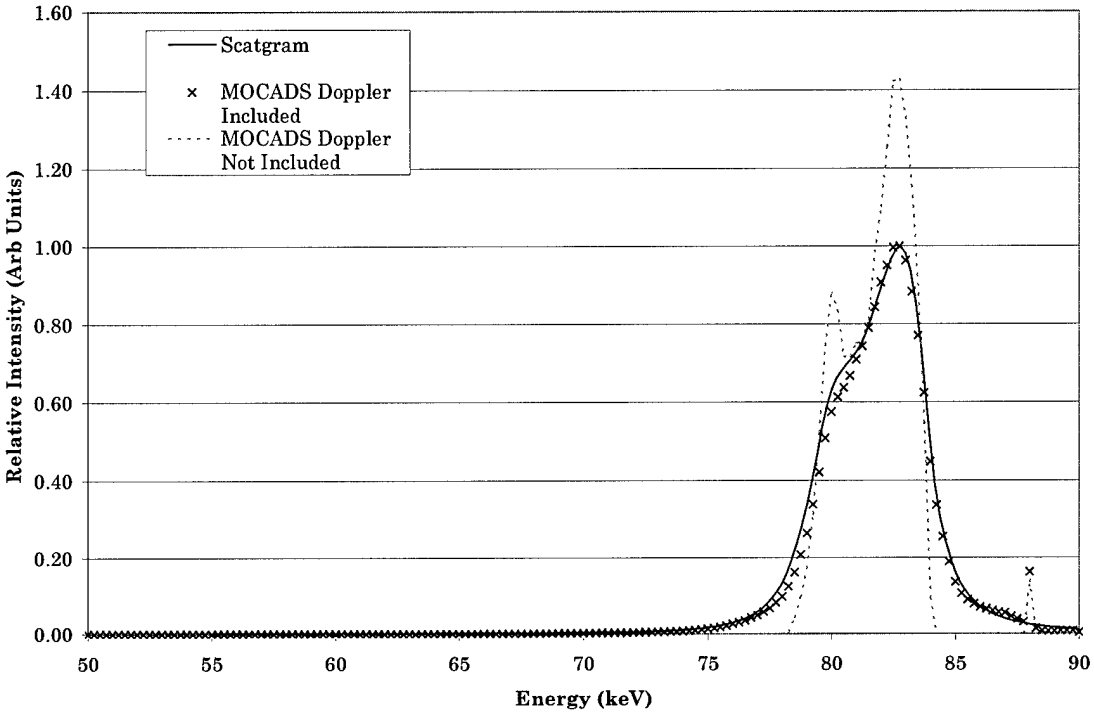

Figure 36: Doppler Broadening when a Void is Included – Detector 4

The results of this validation show that MOCADS is calculating the Doppler-broadened, void characteristics correctly in comparison to Scatgram. Since Scatgram has considerable experimental validation, it should be concluded that MOCADS is correctly calculating the spectrum. These calculations show that MOCADS is reproducing the Doppler broadening correctly when the sample is solid or when the sample includes a void. Although the double scatter portion of the Doppler broadening has not been directly validated, it can be inferred to be correct based upon the single scatter broadening. The inference can be made because the double scatter calculations are simply two successive single scatter calculations.

Chapter 6: Results and Analysis of MOCADS Simulations

The deterministic code, MOCADS, was developed to examine the spectra resulting from double scatter. And, based upon the test cases presented in Chapter 5, the code can be used to examine and analyze the features in the double scatter spectrum. A comparison of the double scatter spectra was made between a case with and without a void in the material. Also, a comparison is presented between the differing results of including Doppler-broadening and polarization to examine the relative effects of these different processes. Finally, the MOCADS-predicted, double scatter spectrum is effective when used on experimental data to recover the single scatter spectrum.

Section 6.1: Results of the Polarization and Doppler Effects

A MOCADS simulation was run to determine the results of polarization and Doppler broadening on the double scatter spectra. Although the polarization could not be directly validated by computer simulations, the method of calculation is so nearly similar as to give confidence in the polarization results. Also, the physical experiment performed was directly compared to the MOCADS calculations with polarization included.

The simulation was a 2 cm x 2 cm x 3 cm sample located a distance of 4 cm from the source. The source collimator was located a distance of 2.54 cm from the source with a height of 2 mm. The four detectors were aligned 4.7 cm from the sample and space 1.95 cm apart. The detector collimator was 0.26 cm from the detectors. The entire sample geometry is shown in Figure **37**.

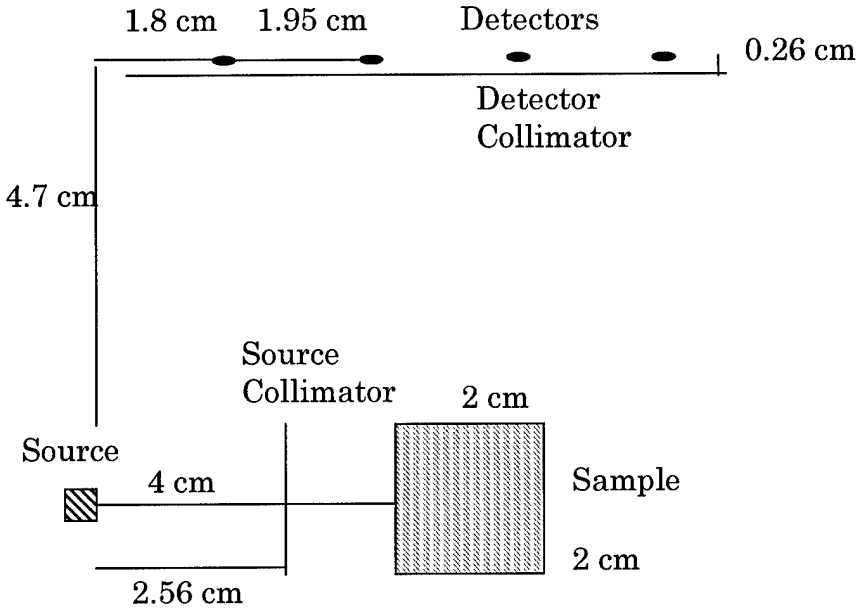

Figure 37: Sample Geometry for Doppler Broadening and Polarization Effects

The MOCADS output was scaled to the first detector such that the sum of the area under the non-Doppler broadened, no polarization curve is equal to one. Thus, all other curves are related to this reference curve.

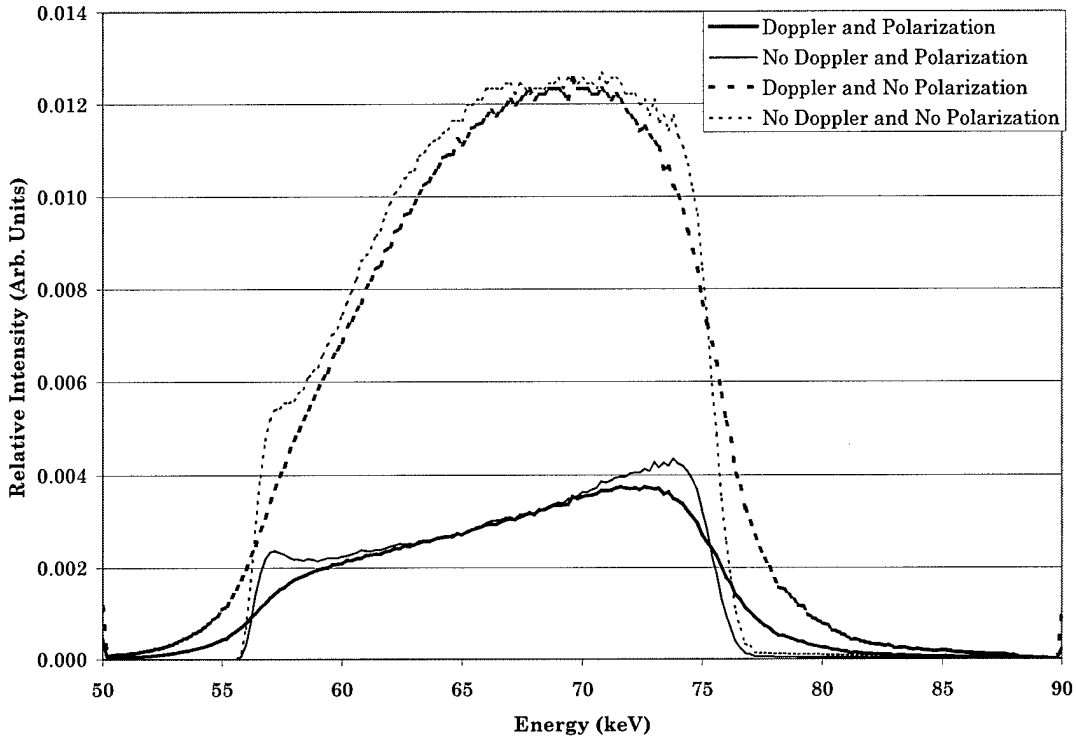

Figure 38: Doppler broadening and Polarization Comparison – Detector 1

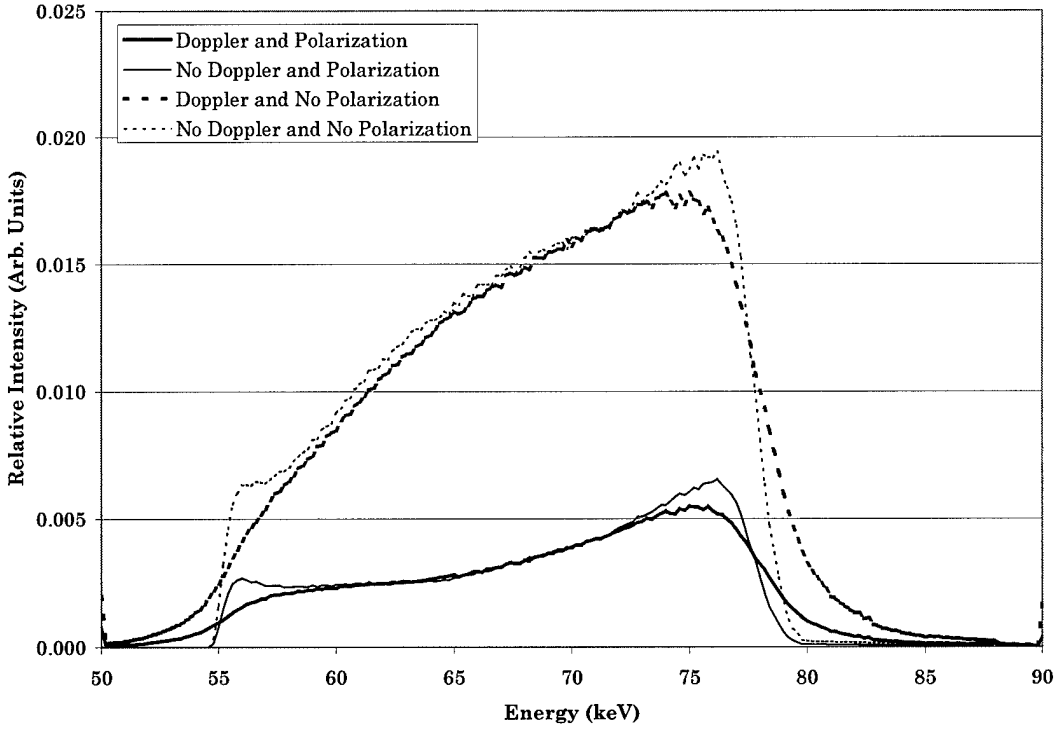

Figure 39: Doppler broadening and Polarization Comparison – Detector 2

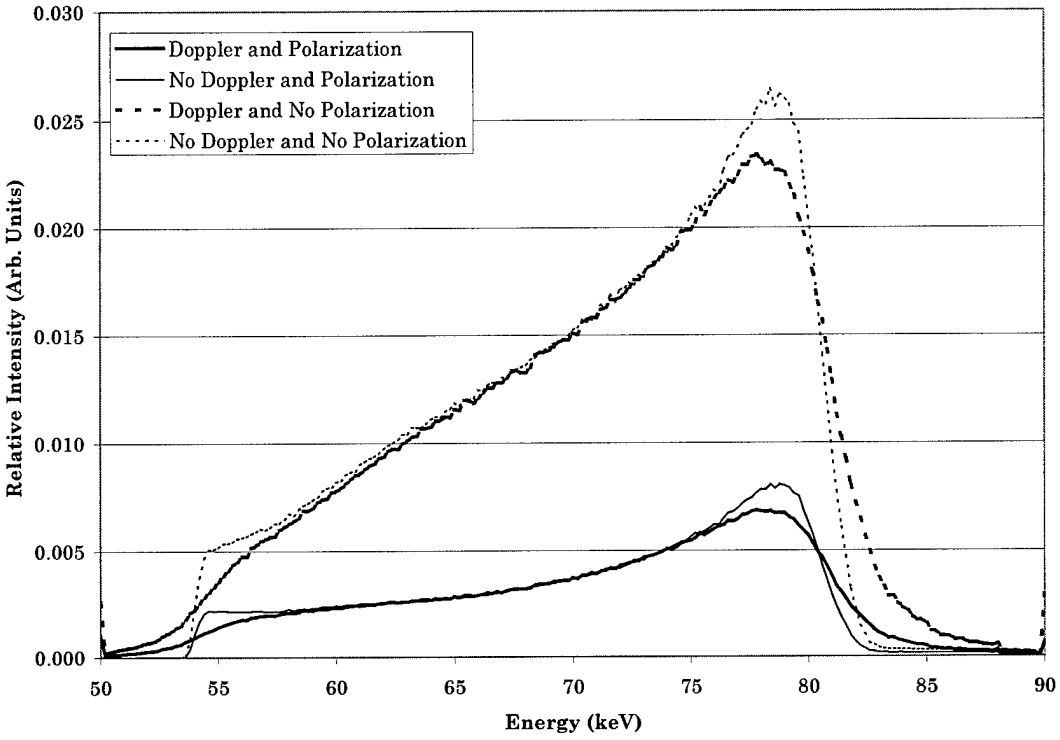

Figure 40: Doppler broadening and Polarization Comparison – Detector 3

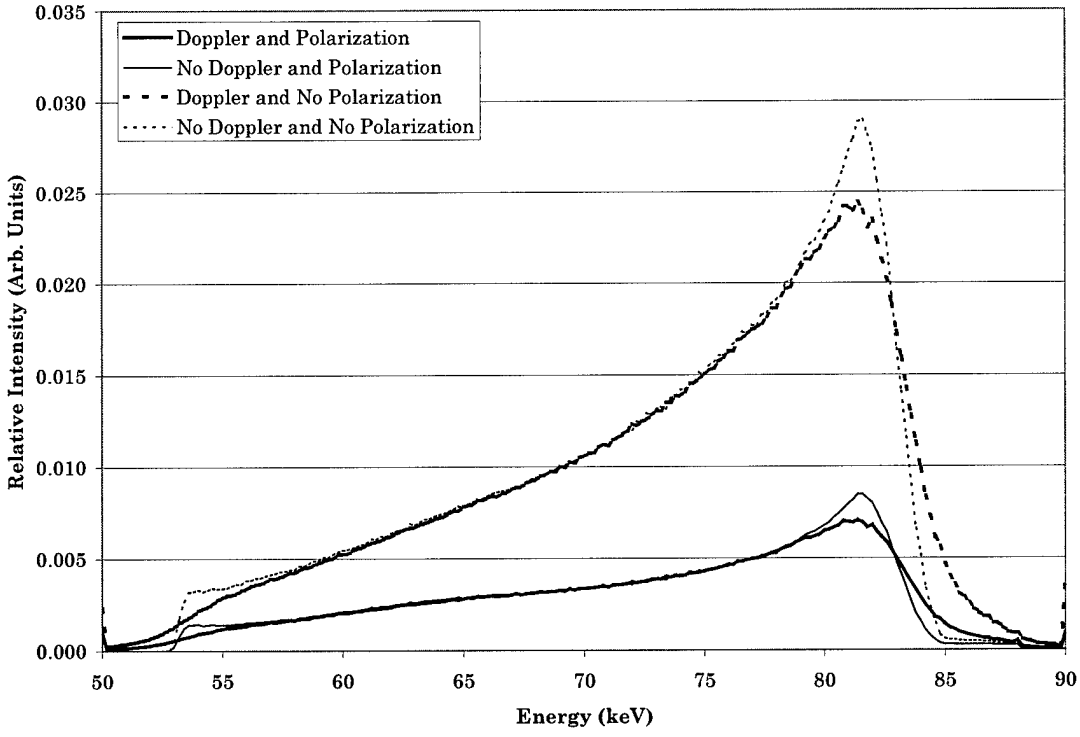

Figure 41: Doppler broadening and Polarization Comparison – Detector 4

These figures show that the polarization influences the shape of the double scatter spectrum. The polarization needs to be included at this energy range in order to determine an accurate spectrum. As the angle between the detector and the sample decrease, the polarization-included spectrum begin to look similar to the spectrum where the polarization was not included. This effect is predicted by equation (13) in Chapter 2. In particular, the Compton-Compton scatter equations predict that at the detector 1 and detector 2 locations, the polarization should play its dominant role. As the detector-sample angle increases towards 180 degrees or decreases towards 0 degrees, the polarization effects should become less pronounced. This analysis is borne out by the last two detector locations having very similar shaped spectra for both polarization-included and not included.

Although the difference between spectra is not as pronounced for the Doppler broadening as for the effects of including polarization, the Doppler broadening is shown to have a consistent influence on the shape of the spectra. The Doppler broadening tends to flatten and widen out the double scatter spectra. This is shown for both the polarization and non-polarization cases. This type of flattening was expected because the Doppler broadening accounts for a very similar flattening in the single scatter spectrum.

For double scatter, then, both the Doppler broadening and the polarization effects need to be included in the double scatter spectrum to

properly determine the correct shape because both effects contribute significantly.

Section 6.2: Results of Double Scatter Void Simulations

A simulation was run in MOCADS to determine the effect of the size of the void on the double scatter spectrum. The simulation did not include the effects of Doppler broadening and polarization. The single scatter spectra were examined to determine whether any change could be detected in the single scatter case.

The simulation was run in a configuration to emphasize any effects of the void on the resultant spectra. The void should be most prominent when the ratio between the volume of the void and the volume of the sample is large. This large ratio between the two represents a worst case scenario for emphasizing the different spectra characteristics.

The configuration has a 2.54 cm x 2.54 cm x 3 cm sample located 6.0 cm from the source. The detectors were aligned 7.54 cm from the sample spaced unequally apart at 5.0 cm, 7.54 cm, 8.81 cm, and 10.0 cm from the source plane. The detector collimator is located 5 cm from the detectors. The source collimator is located 5.0 cm from the source. The geometry is shown in Figure 42. For the void comparison, the same geometry was used except that a 2.2 cm x 2.2 cm void was centered in the sample.

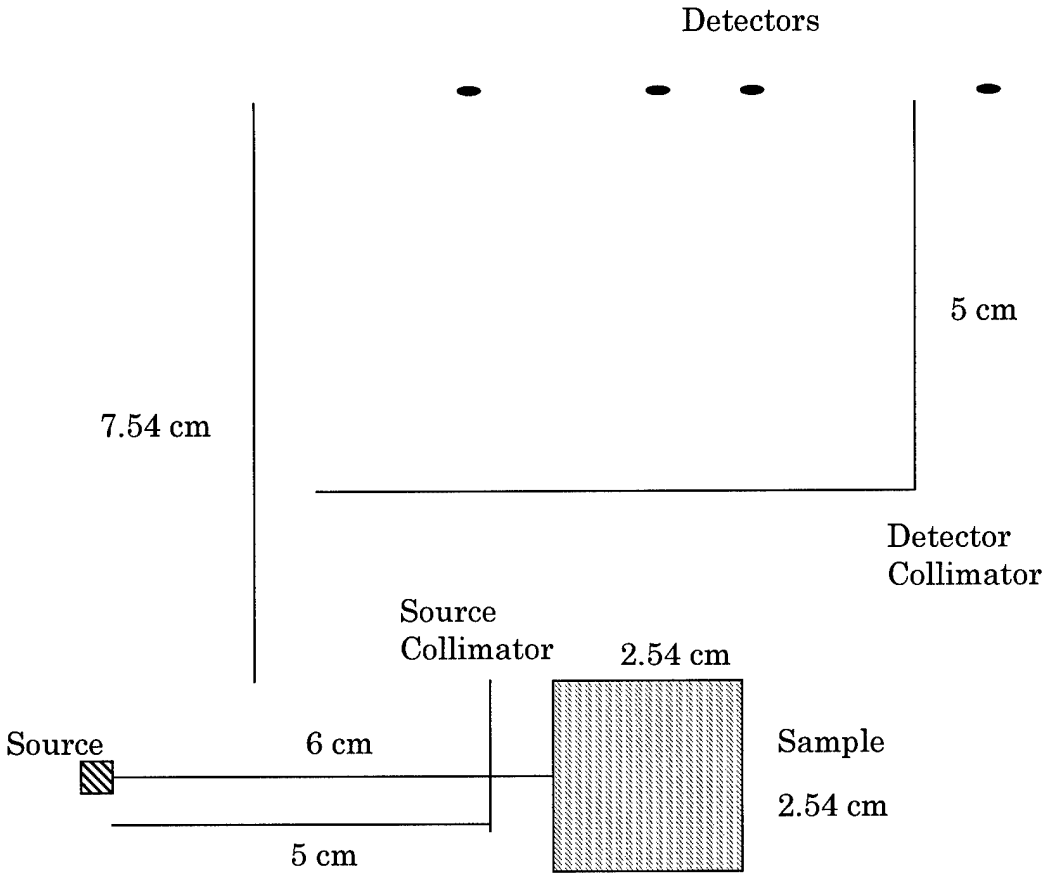

Figure 42: Sample Geometry for Void Comparison

The output from this simulation was scaled such that the area under each spectrum was equal to one. The void and no void simulations were displayed together to show the changes between the two spectra.

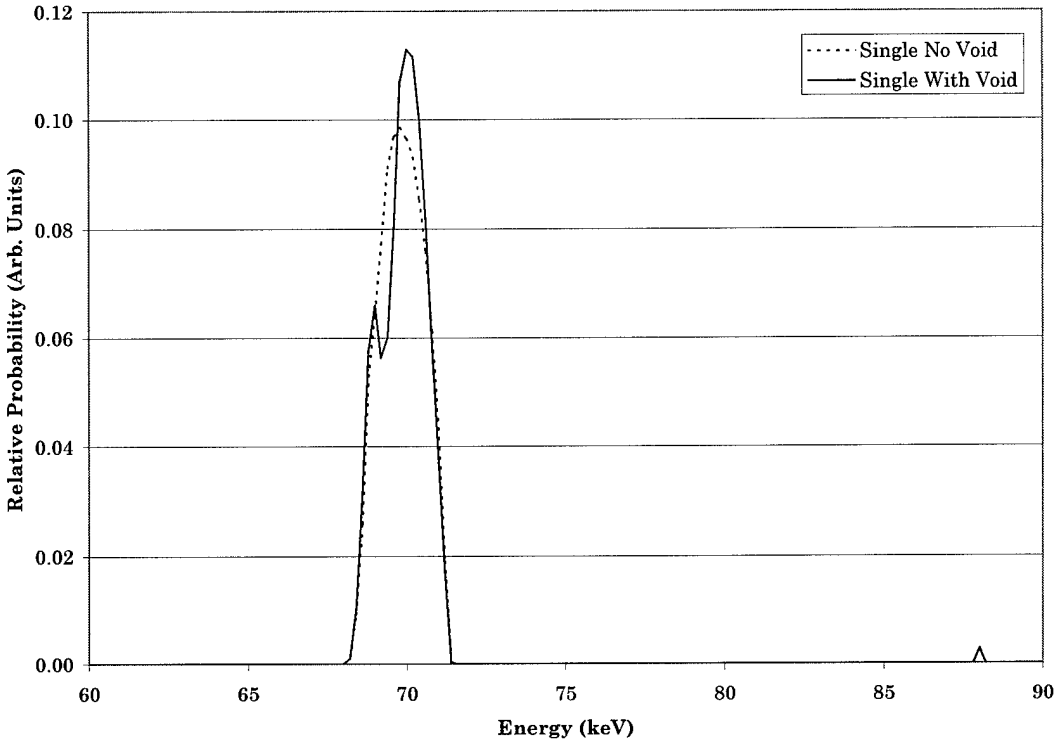

Figure 43: Single Scatter Void Calculations – Detector 1

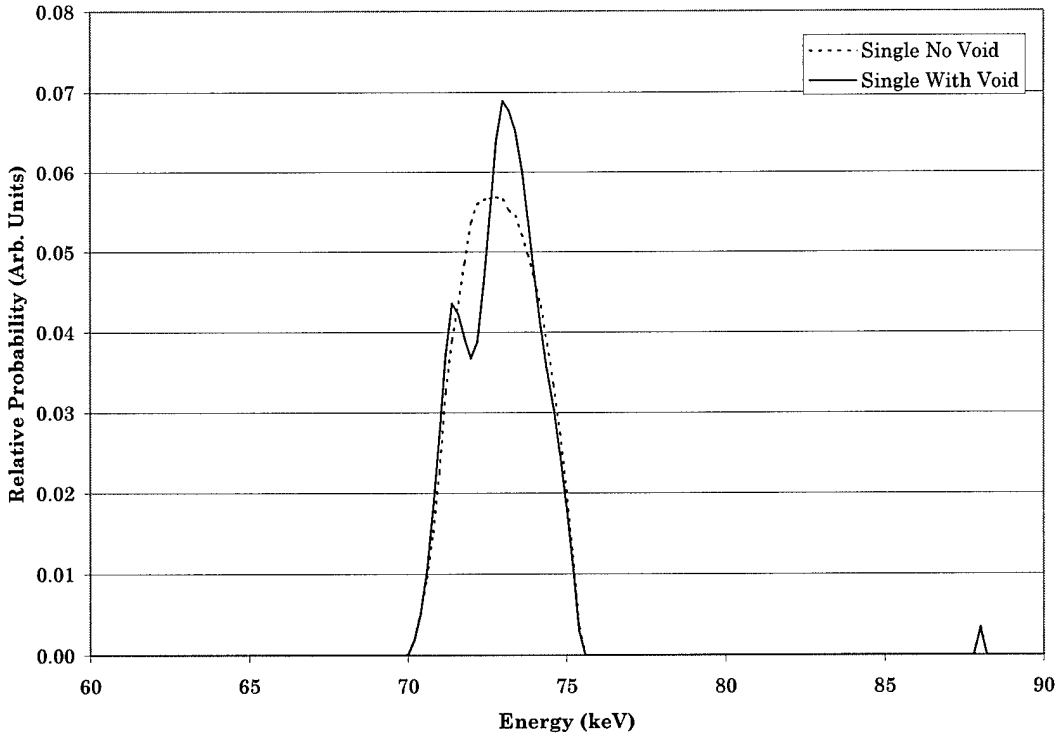

Figure 44: Single Scatter Void Calculations – Detector 2

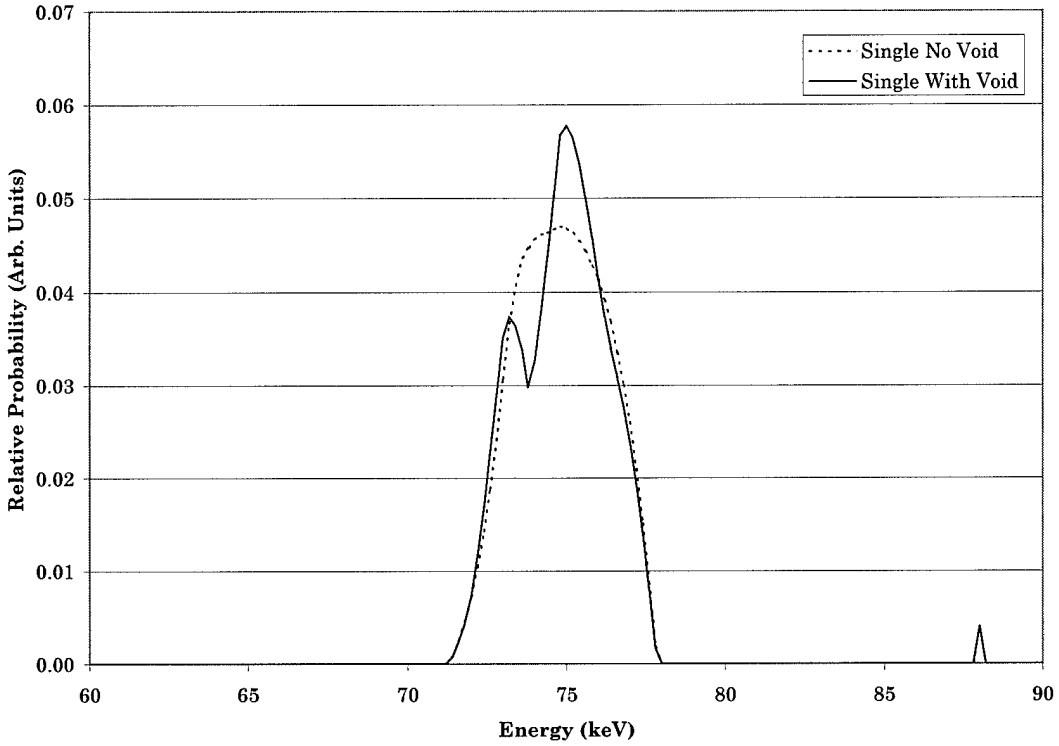

Figure 45: Single Scatter Void Calculations – Detector 3

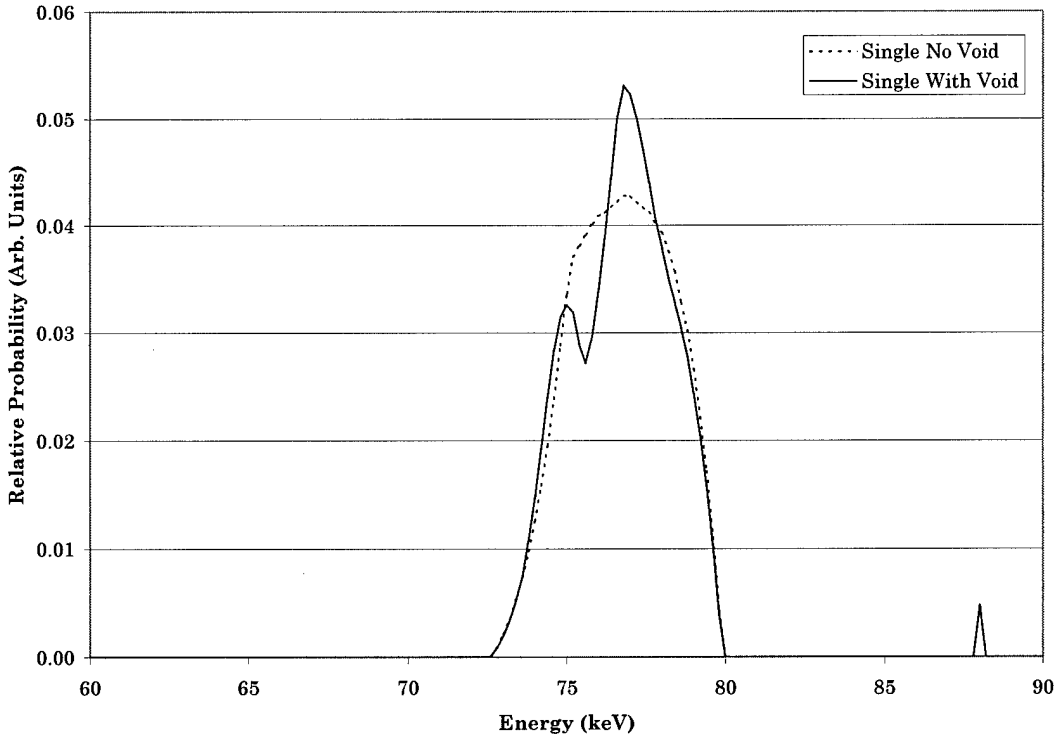

Figure 46: Single Scatter Void Calculations – Detector 4

The single scatter spectra above show that the void changes the single scatter spectra significantly. The small clefts towards the middle of the peaks indicate the presence of the void. Since this void is quite large with respect to the total sample, smaller voids would only cause smaller changes in the single scatter spectra. Indeed, the cleft would become smoother as the void shrinks. Thus, the simulation was chosen to represent a realistic, yet large size void. Indeed, this size is essentially an extreme upper bound for a corrosion flaw.

Figure 47 through Figure 50 represent the same simulation run as for the single scatter results above, but these figures show the double scatter spectrum. This double scatter spectrum is shown without the polarization and Doppler broadening effects included.

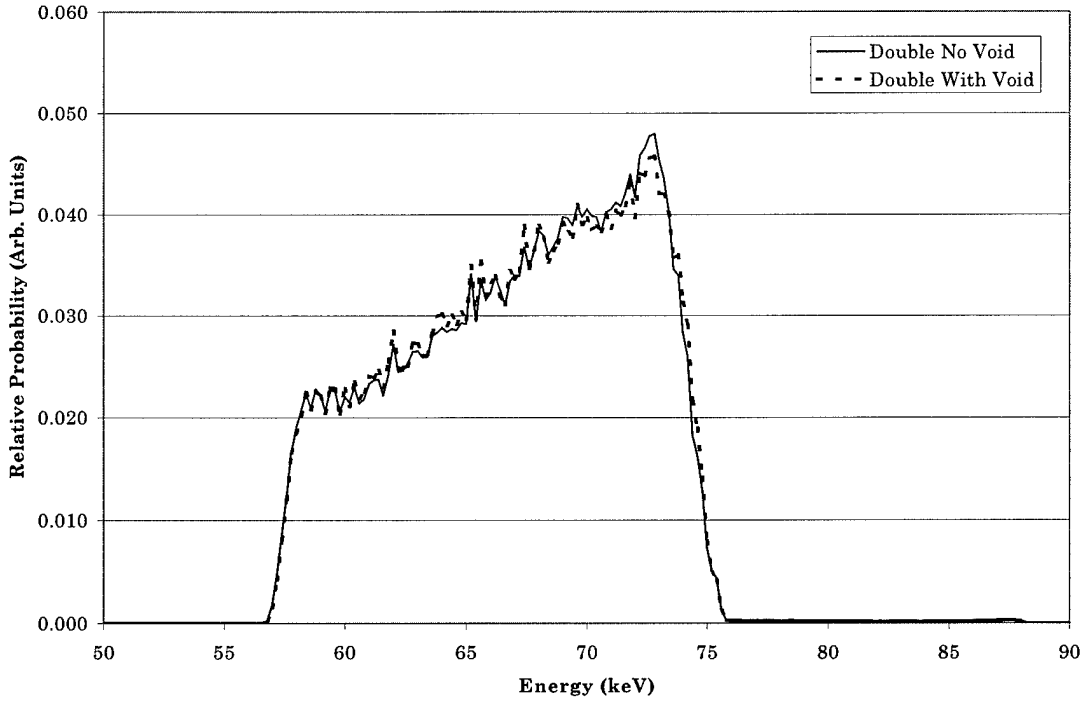

Figure 47: Double Scatter Void Calculations – Detector 1

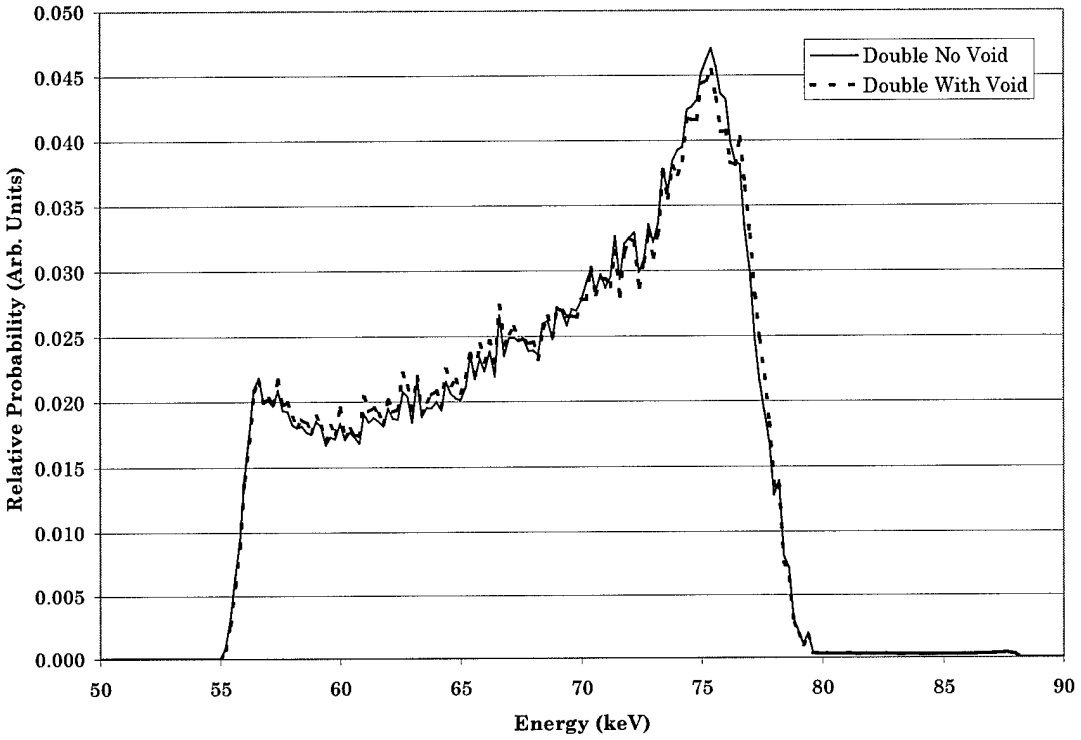

Figure 48: Double Scatter Void Calculations – Detector 2

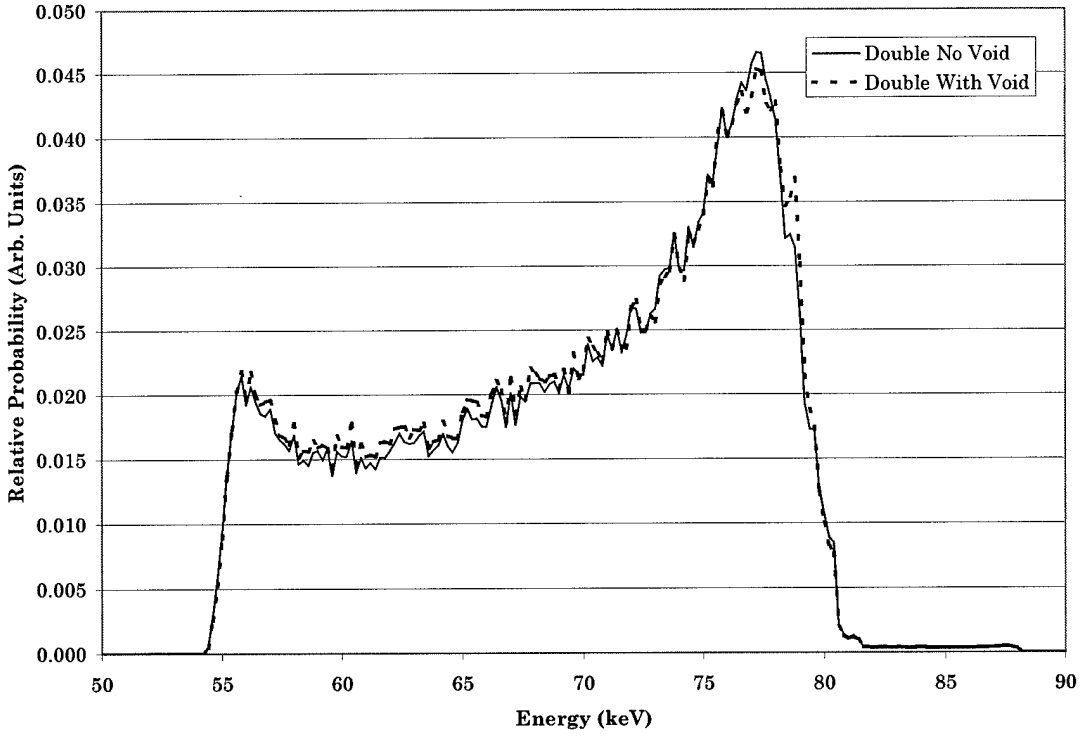

Figure 49: Double Scatter Void Calculations – Detector 3

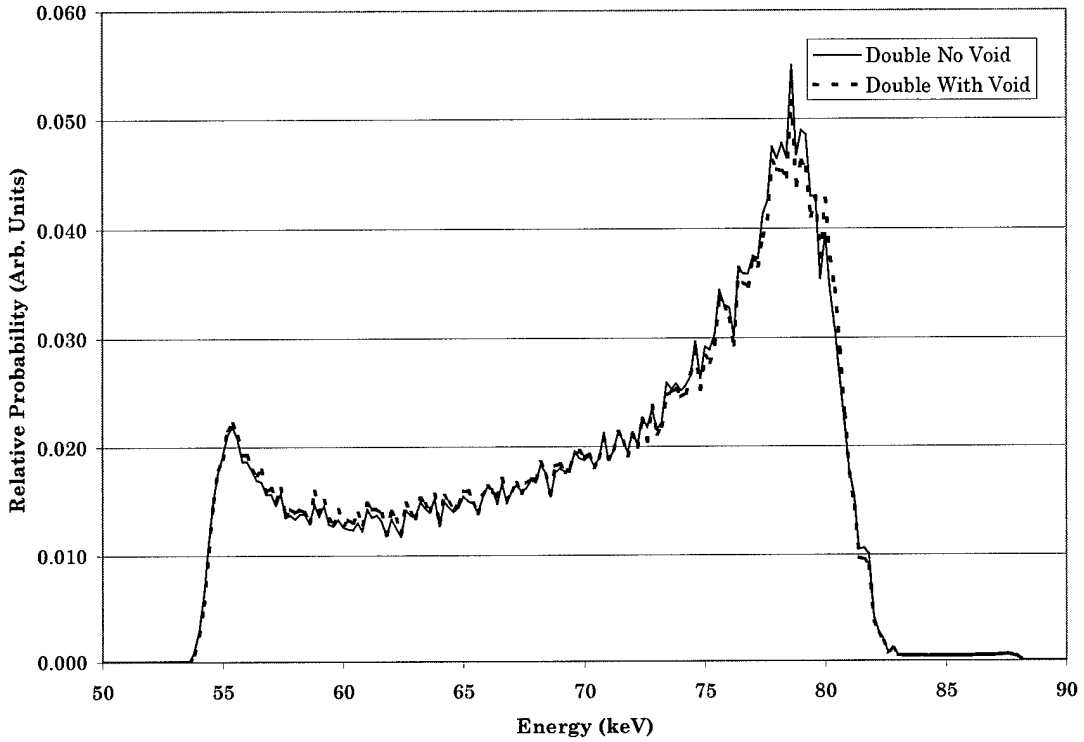

Figure 50: Double Scatter Void Calculations – Detector 4

The comparison between the simulation with and without the void show that the double scatter spectrum has few differences. The differences between the two spectra can be attributed to statistical fluctuations inherent in the Monte Carlo style of integration. Although it would be preferable to smooth these data sets out by sampling the volume more densely, the time required to generate these simulations prohibited further analysis.

This series of simulations show that the void did not affect the double scatter spectrum. Although the example is limited to this simple geometrical configuration, it is assumed that these results can be generalized for most geometries because the void size was chosen large in comparison to the entire sample. Also, the double scatter spectrum was examined for cases where the

collimators had been removed. In these cases, the double scatter spectrum had similar results as above. And, the single scatter spectra for the non-collimated cases did not contain as much structure as collimated case shown above.

The double scatter spectrum depends heavily on the angular placement of the detector-source pair. But, it does not depend on the size of void present in the material. Thus, the subtraction of the double scatter spectrum should be effective regardless of whether or not a void exists in the material.

Section 6.3: Recovering Single Scatter Peak from Experimental Data

An experiment was designed to maximize the multiple scatter spectrum while still having an evident single scatter spectrum. The experiment was carried out in a similar arrangement to the experiment described in Section 5.3. A MOCADS simulation was then run to predict the double scatter spectrum as well as the single scatter spectrum. A comparison was made between the predicted single scatter spectrum and the experimental data without removing the double scatter component. The predicted double scatter spectrum was then subtracted from the experimental results. The remaining spectrum should then be only single scatter and higher order scatters. The net spectrum was then compared to the predicted single scatter spectrum.

The experiment used the 1.095 cm x 1.095 cm x 5.08 cm phantom designed for the validation portion. The plane of the source was offset by 0.635 cm from the plane of the detector. Also, the source was moved .5588 cm closer to the detector relative to the validation geometry. Finally, the phantom was placed at a distance 4.572 cm further from the source. This movement of the phantom away from the detector allowed an overlap between the source and detector viewing planes. This overlap meant that single scatter could reach the detector. The likelihood of single scatter, however, was reduced to approximately that of the double scatter in the peak.

The comparison in Figure 51 shows the uncorrected experimental data with a predicted single scatter as well as the predicted double scatter. The predictions have been scaled visually to the data, trying simply to match the peak height for the single scatter portion. The double scatter was chosen to cross the average value of the experimental data in the region of 66 – 67 keV, where double scatter dominates as in Figure 24. The double scatter component should be dominant in this portion of the spectra based on the previous MCNP predictions for the whole spectra.

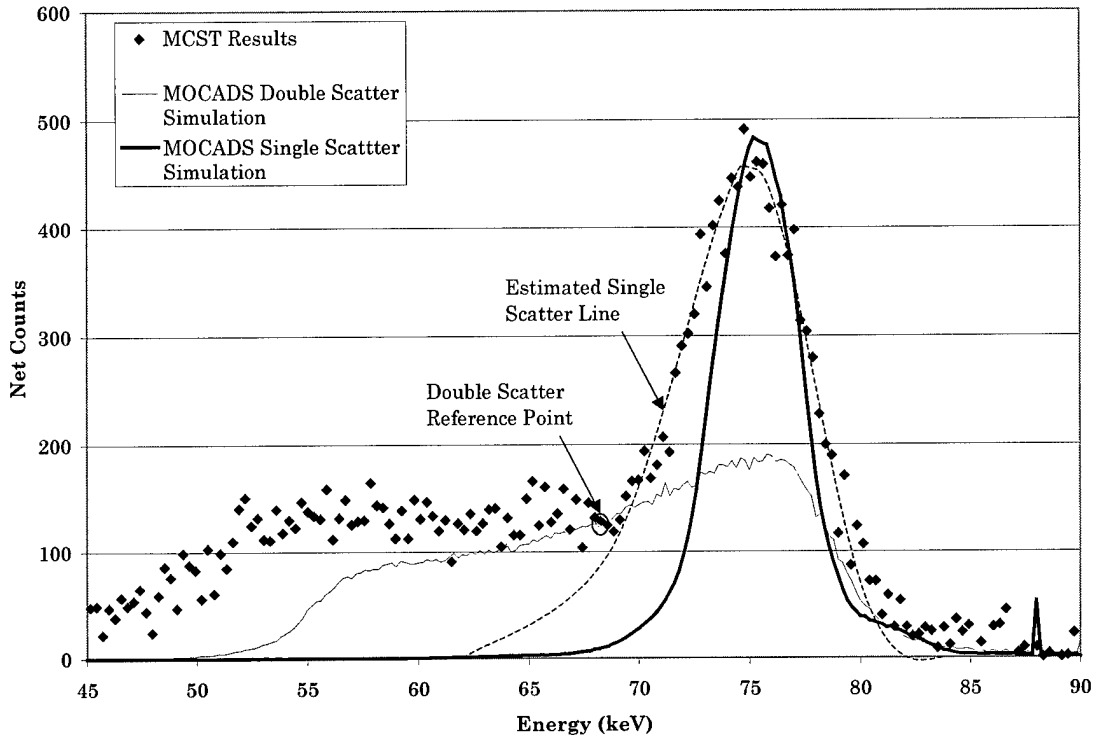

Figure 51: Comparison Between Uncorrected Experimental Data and MOCADS-Predicted Single Scatter and MOCADS-Predicted Double Scatter

Previous to this research, the single scatter peak for this experimental data would have been extrapolated from the dominant scatter peak. Yet as the MOCADS single scatter peak comparison shows, this is a poor approximation—particularly on the lower energy side of the peak. In order to correct for the presence of double scatter, then, it is necessary to subtract out the double scatter component. Figure 52 shows the result of the single scatter peak when the predicted double scatter component has been removed.

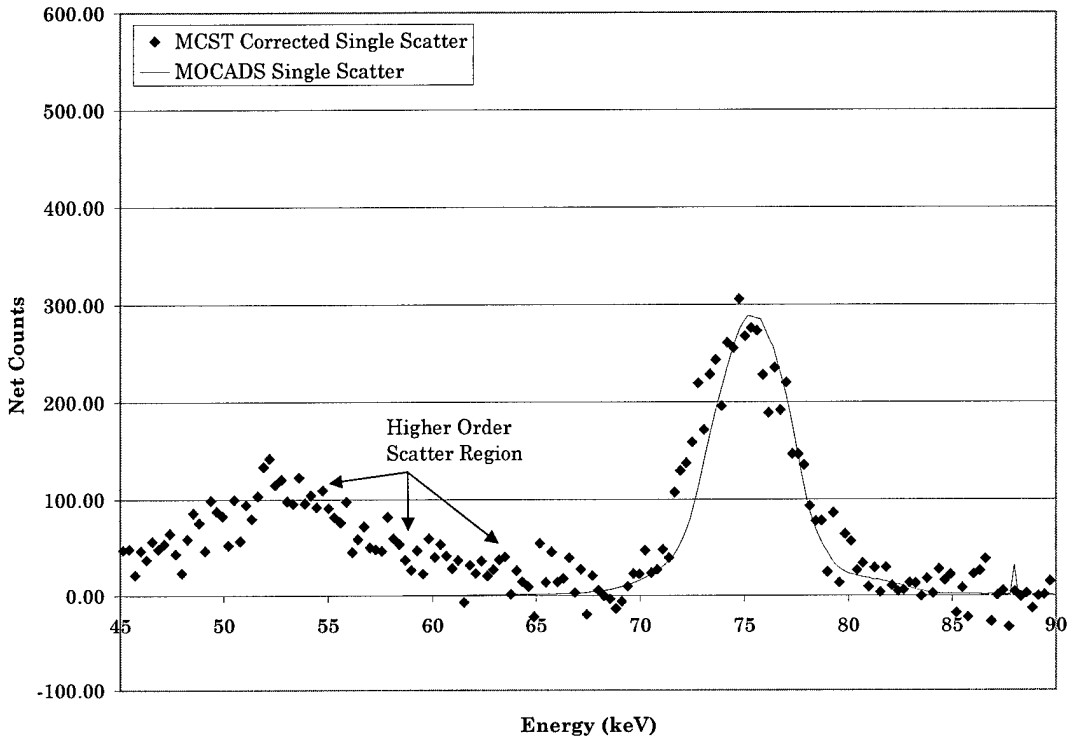

Figure 52: Comparison Between Experimental Data Corrected for Double Scatter and MOCADS-Predicted Single Scatter

The new comparison between the corrected experimental data and the MOCADS-predicted single scatter agree better than the spectra without correcting for the double scatter. Thus, the double scatter spectra can be used effectively to improve the estimate of the single scatter spectra in experimental data.

Chapter 7: Conclusions and Recommendations

Based on the validation and analyzed results, the double scatter spectrum can be characterized and subtracted from the spectrum. The MOCADS code was also effective in determining the double scatter spectrum for specific geometries. Although the code could not predict the exact ratios between the single and double scatters, it was useful when scaled and used to subtract the double scatter spectrum from experimental data. MOCADS was successful in accounting for Doppler broadening and polarization effects.

Section 7.1: Conclusions

When characterizing the double scatter spectrum, it was found that the double scatter spectrum is not dependent on whether the sample contains a void. Although only one geometry was specifically examined, this geometry was chosen to represent a realistic, worst case scenario. The material was only a small shell around a large void region. Yet, even in this worst case, the double scatter spectrum did not show any significant differences between samples with and without the void. Thus, the double scatter spectrum can be properly characterized by only considering the angular placement of the detectors and sample geometry and not by the void size within the sample.

Having obtained a reliable shape for the double scatter spectrum, the subtraction of the double scatter spectrum from the total spectrum was useful

for improving the estimate of the single scatter spectrum. The code accurately predicted the single scatter spectrum shape of experimental data when the double scatter had been removed. The result of the subtraction shows that properly characterizing the double scatter spectrum is essential for recovering the single scatter shape.

Section 7.2: Recommendations

Although MOCADS correctly predicted the shapes and trends of the double scatter, further research on the multiple scatter spectra needs to be performed. The MOCADS code was lacking in several key areas: correctly predicting Rayleigh scatter, which could be due to the MCNP predictions rather than MOCADS, and correctly estimating the ratio between the single and double scatter spectra.

To begin, the Rayleigh scatter portions of the code calculations were not scaled correctly to the prediction made by MCNP. Although some question arose as to MCNP's reliability in the Rayleigh scatter predictions, the difference between the two calculations would need to be resolved. The Rayleigh form factor introduced in Chapter 2 should be compared between the two models. Experiments could be performed to examine only the Rayleigh scatter peaks at 88.03 keV for different angles of scatter to determine the proper angular distribution. Resolving the Rayleigh scatter

discrepancies between MOCADS and MCNP should remove the differences between the two double scatter spectra in the high energy portion.

The Rayleigh scatter experiments may also help with a separate problem with the MCST. The characterization of the *leakage* gamma rays from the source, which penetrate the collimation shielding or other shielding materials. These *leakage* photons are of interest when the photons Rayleigh scatter because it results in an equivalent distributed source. This degradation is related to this double scatter thesis since an initial Rayleigh scatter would distribute the photons differently and may have a characteristic shape that could be characterized directly by MOCADS. Thus, properly characterizing the Rayleigh scatter could improve the entire MCST development.

The failure of MOCADS to accurately predict the ratio between the single and double scatter is due to inaccurate inclusion of constants and the approximation for the $1/r^2$ dispersion. Chapter 3 included a section on the approximation for the $1/r^2$ dispersion. The appoximation could be reexamined to improve the accuracy of the prediction of the ratio between the two types of scatter.

Another approach to improve the ratio between the single and double scatter calculation may be to simply create a fit to the two calculations. A constant fit for the two probability predictions may be possible across many geometries. The fit between the two predictions could be obtained by

comparisons to MCNP calculations as well as more laboratory experiments such as the one described in chapter 6. These two comparisons could yield a constant fitting function.

For further development of the MCST, a new code should be created. The new code should be a Monte Carlo transport code that specializes in the less than 100 keV energy range of interest. MOCADS predicted that the polarization and Doppler broadening would need to be included in this further code development. A modification of the existing MCNP is not recommended due to the very general, overall nature of the code. Yet, other codes exist that perform very specialized photon transport. These codes, EGS4 and Skeptic, could either be modified or used in their entirety. Conversely, since this application is quite specialized, it may be beneficial to develop a Monte Carlo transport code to model the full MCST system.

In addition to predicting the single to double scatter spectrum, a new Monte Carlo transport code could also examine the effects of triple and higher order scatters. These scatters were assumed to be negligible in this work. Yet, the MCNP validation simulation in chapter 5 also included triple and higher order scatters. This spectrum was shown to have a significant impact on the total spectrum. Thus, although the double scatter component is the major source of multiple scatters in the single scatter peak, the characterization of the higher order scatters would need to be accomplished in order to estimate the double scatter accurately from experiment. The

preliminary indications point to a fairly uniform, Gaussian type curve with little dependence on angular distribution for higher order scatters. This correction would greatly aid in the determination of the double scatter spectrum; and, ultimately result in a better estimate of the single scatter spectrum from laboratory experiments to properly image the electron density of the sample.

Bibliography

1. Bell, Friedhelm and Felsteiner, Joshua. "On the correction for multiple scattering of linearly polarized X-rays in Compton profile measurements," Nuclear Instruments and Methods in Physics Research B, volume 101: 379-387 (1995).

2. Biggs, F. and others. "Hartree-Fock Compton profiles for the elements," Atomic Data and Nuclear Data Tables, volume 16: 201-309 (1975).

3. Chomilier, Jacques and others. "Correction for multiple scattering in Compton profile experiments: application for synchrotron source photons," Nuclear Instruments and Methods in Physics Research, volume A235: 603-606 (1985).

4. Dogan, N. and others. "A source reconstruction method for multiple scatter Compton cameras," IEEE Transactions on Nuclear Science, volume 39, number 5: 1427-1430 (October 1992).

5. Duderstadt, James J. and Martin, William R. Transport Theory. New York: John Wiley & Sons, 1979.

6. Ed. by Bradley, David A. "Inelastic scattering of X-rays and gamma rays," Radiation Physics and Chemistry, volume 50, number 1: 1-124 (July 1997).

7. Evans, B. L. and others. "Nondestructive Inspection Using Compton Scattering Tomography," IEEE Transactions on Nuclear Science, volume 45, number 3. 950-956 (1997).

8. Evans, Robley D. "Compton Effect," in Encyclopedia of Physics: Corpuscles and Radiation in Matter II. Ed. S. Flugge. Berlin, Germany: Springer-Verlag, 1958.

9. Evans, Robley D. The Atomic Nucleus. New York: McGraw-Hill Book Company, 1955.

10. Fajardo, P. and others. "Experimental validation of multiple scattering calculations with high energy X-ray photons," Nuclear Instruments and Methods in Physics Research B, volume 134: 337-345 (1998).

11. Felsteiner, J. "Effect of multiple scattering on experimental Compton profiles: a Monte Carlo calculation," Philosophical Magazine, number 30: 537-548 (1974).

12. Felsteiner, J. and Pattison, P. "Multiple scattering and the Compton profile of titanium," Physical Review B, volume 13, number 6: 2702-2704 (March 1976).

13. Fernandez, J. E. "Compton and Rayleigh double scattering of unpolarized radiation," Physical Review A, volume 44, number 7: 4232-4248 (October 1991).

14. Halonen, Vesa and Williams, Brian. "Multiple scattering in the Compton effect. Relativistic cross section for double scattering," Physical Review B, volume 19, number 4: 1990-1998 (February 1979).

15. Knoll, Glenn F. Radiation Detection and Measurement, Second Edition. New York: John Wiley & Sons, 1989.

16. Matscheko, Georg and others. "Compton Spectroscopy in the diagnostic x-ray energy range. II. Effects of scattering material and energy resolution," Phys. Med. Biol., volume 34, number 2: 199-208 (1989).

17. Namito, Y. and others. "Implementation of linearly-polarized photon scatering into EGS4 code," Nuclear Instruments and Methods in Physics Research A, volume 332: 277-283 (1993).

18. Namito, Y. and others. "Implementation of the Doppler broadening of a Compton-scattered photon into the EGS4 code," Nuclear Instruments and Methods in Physics Research A, volume 349: 489-494 (1994).

19. Oak Ridge National Laboratory. Monte Carlo N-Particle Transport Code Sytem: MCNP4B. RSICC Computer Code Collection. US Department of Energy; April 1997.

20. Press, William H. and others. Numerical Recipes in FORTRAN: The art of Scientific Computing, Second Edition. Cambridge: Cambridge University Press, 1992.

21. Ribberfors, R. and Berggren, K.-F. "Incoherent-x-ray-scattering functions and cross sections $(d\sigma/d\Omega')_{incoh}$ by means of a pocket calculator," Physical Review A, volume 26, number 6: 3325-3332 (December 1982).

22. Ribberfors, Roland. "Relationship of the relativistic Compton cross section to the momentum distribution of bound electron states. II. Effects of anisotropy and polarization," Physical Reviw B, volume 12, number 8: 3136-3141 (October 1975).

23. Ribberfors, Roland. "Relationship of the relativistic Compton cross section to the momentum distribution of bound electron states," Physical Reviw B, volume 12, number 6: 2067-2074 (September 1975).

24. Rollason, A. J. and others. "Self-scattering in gamma ray sources used in Compton scattering experiments," Nuclear Instruments and Methods in Physics Research, volume A256: 532-543 (1987).

25. Sakurai, J. J. Advanced Quantum Mechanics. Reading, MA: Addison-Wesley Publishing Company, 1967.

26. Schaupp, D. and others. "Small-Angle Rayleigh Scattering of Photons at High Energies: Tabulations of Relativistic HFS Modified Atomic Form Factors," Journal of Physical Chemistry, Reference Data, volume 12, number 3: 467- (1983).

27. Thomas, George B. and Finney, Ross L. Calculus and Analytic Geometry, Seventh Edition. Reading, MA: Addison-Wesley Publishing Company, 1990.

28. Urban, J. P. and Hosemann, R. "The Compton profile of aluminum with silver K_α fluorescence radiation," Journal of Applied Physics, volume 49, number 1: 392-395 (January 1978).

29. Veigele, WM. J. and others. X-Ray Cross Section Compilation. 1969.

30. Vetterling, William T. and others. Numerical Recipes Example Book (FORTRAN), Second Edition. Cambridge: Cambridge University Press, 1992.

31. Wightman, A. "Note on polarization effects in Compton scattering," Physical Review, volume 74, number 12: 1813-1817 (December 1948).

32. Wood, J. and de Oliveira, C. R. E. "A finite element study of gamma ray transport," Annual Nuclear Energy, volume 17, number 4: 195-205 (1990)

REPORT DOCUMENTATION PAGE	Form Approved OMB No. 0704-0188

1. AGENCY USE ONLY *(Leave blank)*	2. REPORT DATE	3. REPORT TYPE AND DATES COVERED
	March 1999	Master's Thesis

4. TITLE AND SUBTITLE
CHARACTERIZATION OF THE DOUBLE SCATTER SPECTRUM IN MULTIPLEXED COMPTON SCATTER TOMOGRAPHY

5. FUNDING NUMBERS

6. AUTHOR(S)

David W. Gerts, Captain, USAF

7. PERFORMING ORGANIZATION NAME(S) AND ADDRESS(ES)

Air Force Institute of Technology
2950 P Street
WPAFB OH 45433-7765

8. PERFORMING ORGANIZATION REPORT NUMBER

AFIT/GAP/ENP/99M-03

9. SPONSORING/MONITORING AGENCY NAME(S) AND ADDRESS(ES)

AFRL/MLLP
2230 Tenth St, Ste 1
WPAFB, OH 45433-7817
Attention: Dr. Robert Crane

10. SPONSORING/MONITORING AGENCY REPORT NUMBER

11. SUPPLEMENTARY NOTES

12a. DISTRIBUTION AVAILABILITY STATEMENT
Approved for public release; distribution unlimited

12b. DISTRIBUTION CODE

13. ABSTRACT *(Maximum 200 words)*

The Multiplexed Compton Scatter Tomograph (MCST) uses single back-scattered photons to image electron density in aluminum. A source of error in this imaging technique is the presence of multiple scatters. This thesis studies the double scatter spectrum as an approximation of the multiple scatter spectrum. A deterministic code called Monte Carlo Double Scatter (MOCADS) was developed to investigate the double scatter spectrum.

The code includes calculations of the Rayleigh scatter, Compton scatter, Doppler broadening effects of the spectrum, and polarization effects following the Compton scatter. The Doppler broadening portion of the code was validated by a deterministic code called Scatgram. The mechanics of double scatter were validated by a Monte Carlo transport code. And all included features in the code were validated by a laboratory experiment.

The MOCADS code was used to simulate an experiment where a void was present in the sample and compared to a solid sample. The simulation showed that the shape of the double scatter spectrum did not depend of the presence of the void. Another simulation examined the effects of polarization and Doppler broadening. These two effects were shown to significantly influence the shape of the spectrum. Finally, a laboratory experiment was examined where the single scatter estimate was improved by the removal of the double scatter spectrum from the total spectrum.

14. SUBJECT TERMS
Compton Scatter, Double Scatter, Multiplexed Compton Scatter Tomograph, Gamma Scatter Spectrum, Polarization Effects in Compton Scatter, Doppler Effects in Compton Scatter

15. NUMBER OF PAGES
108

16. PRICE CODE

17. SECURITY CLASSIFICATION OF REPORT	18. SECURITY CLASSIFICATION OF THIS PAGE	19. SECURITY CLASSIFICATION OF ABSTRACT	20. LIMITATION OF ABSTRACT
UNCLASSIFIED	UNCLASSIFIED	UNCLASSIFIED	UL